CORRELATING MALDI-IMS AND MRI DIFFUSION MEASUREMENTS IN THE C6 RAT GLIOMA TUMOR MODEL

By

AMELIE R. GILLMAN

Thesis

Submitted to the Faculty of the

Graduate School of Vanderbilt University

in partial fulfillment of the requirements

for the degree of

MASTER OF SCIENCE

in

Biomedical Engineering

May, 2009

Nashville, Tennessee

Approved:

Professor John C. Gore

Dr. Tuhin K. Sinha, Ph.D.

ACKNOWLEDGEMENTS

I would like to express my gratitude to the sources of funding which enabled the work presented in this thesis. The generous financial support of the National Institutes of Health Predoctoral Training Grant T32 EB01628 and the Department of Defense Breast Cancer Research Program of the Office of the Congressionally Directed Medical Research Programs Predoctoral Traineeship Award BC073628 has provided for the time, equipment, and materials necessary to conduct this study. In addition, the Harold Stirling Vanderbilt Fellowship providing funding to support completion of didactic coursework which helped to establish a framework of knowledge upon which to base this investigation.

I am eternally grateful for the opportunity to work with my mentors, Drs. John Gore, Ph.D., Tuhin Sinha, Ph.D., and Thomas Yankeelov, Ph.D. Their guidance, wisdom, patience, and kindness have been continuous sources of inspiration and motivation. Dr. Gore's input with regards to the direction of this study has reflected unparalleled expertise in the field of imaging science. Dr. Yankeelov's mentorship has been incalculable in helping me to understand the physiological aspects of cancer imaging; and Dr. Sinha's analytical genius has provided the foundation upon which to quantify such phenomena.

I am also deeply appreciative of the assistance of my fellow graduate students Mary Loveless, Daniel Colvin, and Zhengyu Yang in the collection and analysis of data for this project. Institute of Imaging Science staff members Zoe Yue and Jarrod True provided invaluable help with animal handling. Erin Seeley in the Mass Spectrometry

Research Center helped with acquisition of protein measurements, as well as with specimen preparation. This work would not have been possible without them.

Dr. Wellington Pham, Ph.D., has been a source of encouragement and support during my graduate career. I am grateful to him, as well as to Drs. Charles Manning, Ph.D., and Todd Peterson, Ph.D., for extending me opportunities to work on distinct yet inter-related projects which helped me to achieve a more comprehensive understanding of the field of imaging science.

To my loved ones, especially Cheyenne and Rob, your unwavering support and belief in me have been the impetus to grow and the foundation upon which I stand as I become the person I strive to be.

TABLE OF CONTENTS

Page

LIST OF FIGURES

LIST OF TABLES

Table Page

CHAPTER I

CORRELATING MALDI-IMS AND MRI DIFFUSION MEASUREMENTS IN THE C6 RAT GLIOMA MODEL

Introduction

This year, it is estimated that more than 1.4 million Americans will be diagnosed with cancer and that at least 1,500 will die each day from the disease [6]. Worldwide, one in eight deaths are currently attributable to some form of cancer; and the impact of cancer on global health is anticipated to rise as the population ages and grows [7]. While advancements in diagnosis and treatment methods have yielded an increase in five-year cancer survival rates from 50% in 1976 to 66% in 2000 [6], the changes in gross tumor morphology which are interrogated by current radiological methods to determine treatment efficacy are often unable to report detailed information on tumor status [3, 4, 8] indicative of early treatment response [1, 2, 9]. Thus, current methods for assessing cancer treatment response may be improved by the use of repeatable and non-invasive imaging techniques which provide quantitative measurements of tumor status and insights into basic molecular and cellular processes within tissues. The early application of such methods of tissue characterization would permit clinicians to tailor therapy on an individual basis based on each patient's response to a particular agent.

Specific macromolecules have been determined to be involved in processes such as cell turnover [10 – 12] and angiogenesis, which are crucial for cancer growth [8, 13, 14]. Consequently, the up-regulation of numerous proteins has been associated with tumorigenesis and established as an independent indicator of patient prognosis in several

kinds of cancer [1, 2, 9]. The study presented in this thesis is motivated by the theory that the ability to non-invasively identify signatures of up-regulated proteins in cancerous tissue would facilitate further molecular studies and discovery of unknown biomarkers of cancer. The overarching goal of this work is to examine the spatial correlation between noninvasive magnetic resonance imaging (MRI) metrics and their underlying quantifiable molecular-level physiological processes which cannot be obtained noninvasively. Thus, an interdisciplinary approach, drawing on aspects of cancer biology, imaging technology, and computational, mathematical, and chemical analyses is employed to address the following core study components:

Objective: To enhance the understanding of the molecular-level influences on diffusion maps provided by MRI in the C6 rat glioma model of brain cancer.

Hypothesis: It is hypothesized that tumor protein signatures in C6 rat gliomas correlate spatially with tumor diffusion measurements and cellularity.

Specific Aims

Specific Aim 1: Development and automation of techniques for co-registration of *in vivo* diffusion-weighted MRI and *ex vivo* matrix-assisted laser desorption (MALDI) measurements.

Specific Aim 2: Statistical analysis of co-registered measurements to determine the correlation between levels of specific tumor-expressed proteins and water diffusion rates reported by MRI.

A discussion of features of the above-mentioned fields which are relevant to this study is presented next.

Background

The C6 Glioma Rat Tumor Model

The C6 Glioma cell line is often used in rats as a model of brain cancer [15] which is morphologically similar to human glioblastoma multiforme (GBM) [8], an aggressive cancer of the glial cells with a median patient survival of less than one year [16]. In general, rodent models of brain cancer maintain several important aspects of the complexity of the disease, including inflammatory response and neovasculature development [8]. Moreover, intracranial injections of C6 cells into Wistar rats in particular yield solid malignant tumors which develop necrotic cores and display a level of polymorphism characteristic of human GBM [8]

C6 cells grow preferentially around blood vessels, with invasiveness directed along neuronal fibers [8]. Unfavorable cellular microenvironmental factors prevent mitosis of isolated mobile C6 cells in Wistar rats [8]. Thus, invasion of surrounding brain tissue is accomplished not by cellular proliferation but *via* an alternate method in which individual C6 cells release proteolytic enzymes that generate micropockets which

degrade the extracellular matrix [8]. Degeneration and remodeling of the basement membrane facilitates angiogenesis, providing increased delivery of oxygen and nutrients from the neovasculature to the primary tumor [8].

Several proteins have been identified in association with the cell-cell and cell-matrix interactions crucial to C6 cellular invasion and angiogenesis, including vascular endothelial growth factor (VEGF), basic fibroblast growth factor (bFGF), matrix metalloproteinase II (MMP2), as well as various adhesion molecules, proteases, and cytokines [8]. Of note, commonly used chemotherapies which target actively proliferating tumor cells are less effective in the prevention of C6 cell invasion than therapeutic agents which disrupt cytoskeletal assembly [8].

Diffusion and Cellularity in Healthy and Cancerous Tissues

Water molecules in solution undergo random, thermally-induced movement referred to as self-diffusion or Brownian motion [17, 18]. Although the net displacement of water molecules diffusing through tissue is zero, the path length traversed by individual water molecules is time-dependent and can be described by

$$\left\langle r^2 \right\rangle = 2DT\,, \qquad \textit{(Equation 1)}$$

where $\left\langle r^2 \right\rangle$ is the square of the average path length, D is the rate or coefficient of diffusion (3.0×10^{-3} mm^2/s for pure water at 37º Celsius [17, 19]), and T is the time of observation of the water molecule's motion [18]. For water in cellular tissues, D is found to be much lower than that of water in free solution [17].

Physiologically, the diffusion of water molecules in brain tissue is restrained by the presence and degree of permeability of structures within the tissue that inhibit the

mobility of water molecules. Examples of such barriers include cell membranes, white matter tracts, proteins, and collagen fibers [20]. Since tumor growth is characterized by unchecked cellular proliferation, the development of tortuous vasculature, and upregulation of proteins associated with the generation of these features, the self-diffusion of water molecules in cancerous tissues often varies from that of healthy, well-organized tissues of the same type. Thus, by examining the rate of water diffusion in a particular tissue, certain features characteristic of the nature of barriers encountered by the diffusing water molecules may be studied. Specifically, cellularity, which characterizes the number and state of cells in a given tissue volume, has been found to correlate inversely with the diffusion rate of water in breast, brain, and renal cancers [20 – 23].

Quantitatively, cellularity may be defined as the ratio of the total area of tumor cell nuclei relative to the total area of the tissue of interest [24]. Since cell membranes can serve as effective barriers to diffusing water molecules, increases in cell density result in restricted water diffusion, while decreases in the number of cells in a given tissue region reduce the number of barriers, therefore resulting in less restricted diffusion of water. Thus, determination of the diffusion rate of water molecules for a given type of tissue provides a means by which cell density may be assessed [17].

Measuring Diffusion via MRI

The rate of self-diffusion of water in tissue is described by an apparent diffusion coefficient (ADC) measured in units of area/time. The ADC can be measured noninvasively *via* modification of a traditional magnetic resonance imaging (MRI)

excitation technique, the spin-echo pulse sequence [25, 26]. Spin-echo pulse sequences, depicted in Figure 1 (Panel A), begin with the application of a 90º radiofrequency (RF) pulse to establish spin phase coherence in the transverse plane (relative to the direction of the applied static magnetic field) [27]. After some time, T (on the order of tens to hundreds of ms), dephasing occurs due to the effects of spin-spin interactions and magnetic field inhomogeneities [27]. A 180º RF pulse is then applied to nutate the spin precession to its mirror image [27]. After passage of an additional time T, phase coherence is re-established, producing the maximum MR signal acquired at time *TE* [27].

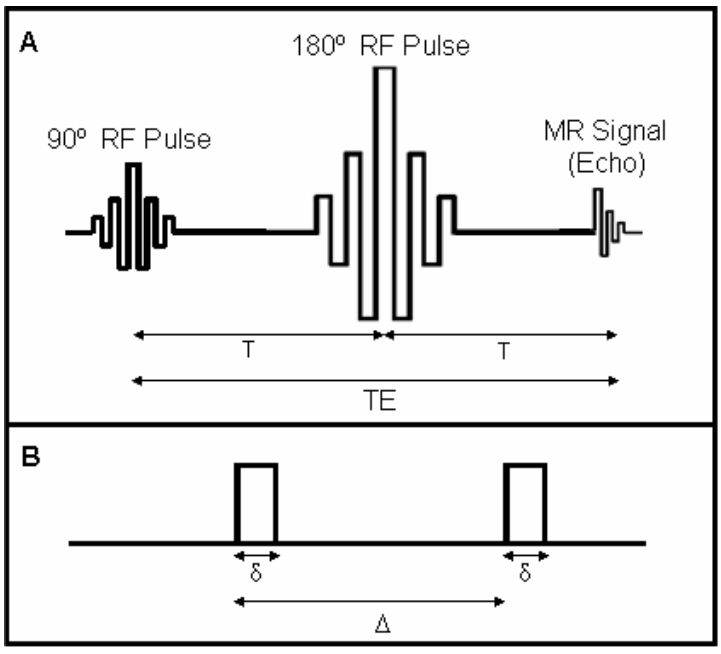

Figure 1: Spin-echo and diffusion-weighted MRI pulse sequences. Spin-echo pulse sequences (Panel A, top) utilize 90º and 180º RF pulses to achieve maximum spin phase coherence and consequent maximum MR signal intensity. Diffusion-weighting is accomplished *via* application of spatially-varying diffusion gradients before and after the 180º RF pulse (Panel B, bottom). The first gradient causes a spatially-dependent change in phase, while the second gradient reverses the phase change to an extent due to molecular mobility. Phase dispersion in locations of mobile molecules yields attenuation of MR signal intensity, thus indicating regional relative diffusion rates.

Diffusion weighting of the spin-echo pulse sequence involves application of two equal diffusion gradient pulses before and after the 180º pulse, as indicated in Figure 1 (Panel B), [25, 26]. The incorporation of diffusion gradients results in diffusion-dependent attenuation of the MR signal intensity *via* the mechanisms described below and illustrated in Figure 2.

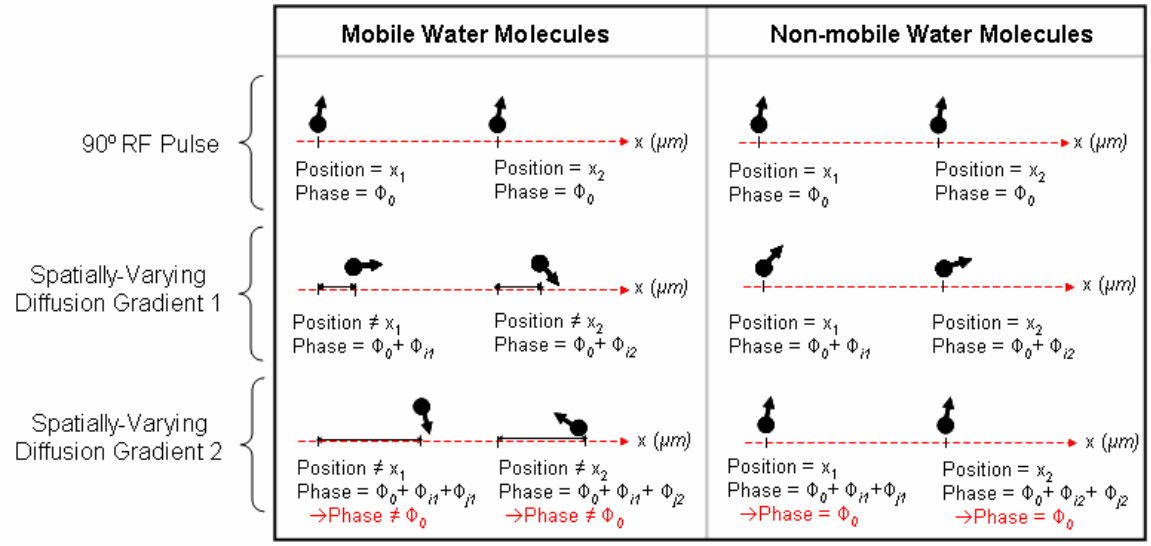

Figure 2: Effects of diffusion gradient application on phase coherence for a pair of mobile molecules and a pair of non-mobile water molecules in one dimension. After the 90º RF pulse, water molecules (blackened circles) at all positions, x, possess identical phase, ϕ (indicated by the direction of the black arrows), as shown in the top panel. At some time, t, before application of the spin-echo 180º RF pulse (not shown), a spatially-varying diffusion gradient is applied, generating a spatially-dependent change in phase of the water molecules (middle panel) at each position x. At a time t after application of the spin-echo 180º RF pulse, a second diffusion gradient is applied (bottom panel) which negates the phase-changing effects of the first diffusion gradient on stationary water molecules (bottom right) yet amplifies phase decoherence of diffusing water molecules (bottom left). Since maximum MR signal intensity is obtained in regions of full phase coherence, tissue regions characterized by high water mobility demonstrate attenuation in localized MR signal intensity; whereas tissue regions of low diffusion generate signal intensities similar to those which would have been generated in the absence of diffusion gradient application.

Consider a set of hydrogen atoms located within water molecules in biological tissue. The protons possess spins which are in phase immediately after the application of

the 90º rephasing pulse (Figure 2, top panel) [18]. After some time, typically tens of ms [17], a spatially varying diffusion gradient is applied (Figure 2, middle panel) such that a spin at position x_i acquires an additional phase component, ϕ_i, given by

$$\phi_i = -\gamma x_i G_x \delta , \qquad \textit{(Equation 2)}$$

where γ is the gyromagnetic ratio, G_x is the amplitude of the diffusion gradient, and δ is the duration of the diffusion gradient pulse. A second diffusion gradient, applied after the 180º pulse (Figure 2, bottom panel), causes the spins at position x_j to acquire a second additional phase component, ϕ_j, where

$$\phi_j = \gamma x_j G_x \delta . \qquad \textit{(Equation 3)}$$

Thus, for non-mobile water molecules with $x_i = x_j$ and ϕ_i=-ϕ_j, the absence of a resulting net phase change yields a signal intensity similar to that which would have been obtained without diffusion weighting [18]. However, for diffusing water molecules, $x_i \neq x_j$ and $\phi_i \neq \phi_j$, causing these molecules to experience a net phase difference, $\Delta\phi$, given by

$$\Delta\phi = \gamma G \delta (x_j - x_i) . \qquad \textit{(Equation 4)}$$

Within any volume of tissue, there will be signal contributions from multiple values of $\Delta\phi$, which interfere destructively and cause signal "dephasing." This dephasing results in localized loss of signal intensity in displaced water molecules in the tissue being imaged [18].

The measured MR signal intensity, S, obtained from the spin-echo and diffusion-weighted pulse sequences are

$$S = S_0 (1 - e^{-TR/T_1}) e^{-TE/T_2} \qquad \textit{(Equation 5)}$$

and

$$S = S_0(1 - e^{-TR/T_1})e^{-TE/T_2}e^{-b \bullet ADC} \qquad \textit{(Equation 6)}$$

respectively, where S_0 is the signal intensity prior to application of field gradients; *TR* and *TE* are the pulse repetition and echo times, respectively; T_1 and T_2 are the longitudinal and transverse relaxation times, respectively, of the bulk magnetization vector. The *b*-value is a variable which reflects the strength and duration of the diffusion-sensitizing gradient. The gradient amplitude, G_x, duration, δ, and temporal spacing, Δ (not to be confused with the change in phase, Δ, of Equation 4), between the applications of the first and second diffusion gradients are incorporated into the *b*-value as given by [25]

$$b = (\gamma G)^2 \delta^2 (\Delta - \frac{\delta}{3}). \qquad \textit{(Equation 7)}$$

The ADC can be calculated *via* linear regression analysis, with the applied *b*-values as the independent variable and the logarithm of the ratio of signal intensities of MR datasets collected at multiple *b*-values, $S(b)$, to the non-diffusion weighted signal intensities, S, as the dependent variable [28]. The ADC at each voxel is the slope of the linear fit, which may be rearranged to be defined by

$$ADC = -\frac{1}{b} \ln \frac{S(b)}{S}. \qquad \textit{(Equation 8)}$$

Since the magnitude of diffusion weighting in MRI is dependent upon the applied *b*-value, several considerations are important in selecting which *b*-values to use in determination of ADCs. First, signal intensity measurements incorporate diffusion gradient spacing and duration (Δ and δ, respectively, in Equation 7) which must provide adequate time for diffusing water molecules to encounter barriers [29]. That is, for short

measurement times, the distances traversed by mobile water molecules may be insufficient for them to arrive at diffusion boundaries, thus yielding measurements which result in high ADCs that do not reflect cellularity [29]. In addition, the use of low *b*-values (less than 300 s/mm^2) may result in overestimation of ADCs due to low *b*-value sensitivity to the motion of rapidly moving water molecules, such as those in blood vessels and microvasculature [30, 31].

Larger *b*-values (greater than 1200 s/mm^2) may also yield overestimated ADC values and consequent signal loss, due to their necessity for larger repetition times which increase the incidence of motion artifacts and decrease the signal-to-noise ratio (SNR) [30, 31]. Nevertheless, larger *b*-values provide greater sensitivity to slower-moving molecules in both intra- and extra-cellular spaces [31], and may be of greater use in determination of therapeutic response in cellular tissues, owing to the relative insensitivity of larger *b*-values to diffusion in highly edematous tissues [17]. Of note, the use of relatively short echo times improves SNR, yet limits the range of *b*-values which may be applied during image acquisition (see Figure 1) [31]. Overall, many studies of microstructural tissue characteristics by diffusion-weighted imaging have employed *b*-values ranging several orders of magnitude, from 0 s/mm^2 (T_2 weighted) up to several thousands of s/mm^2 [17, 31-36].

While many considerations affect diffusion of water in biological tissues, the ADCs of brain tissue exhibit particular complexity, due to the heterogeneous structure of both healthy and pathologic brain tissue. For example, the diffusion rate of water is much lower in regions characterized by densely packed fiber tracks, such as white matter and the corpus callosum, than in water-rich regions scarce in barriers to diffusion, such as

the ventricles [26, 37]. Further confounding factors are present when tumor growth affects the ADC of white matter tracts by disrupting their structural integrity [37]. Moreover, the ADCs of brain tumors may vary across the extent of the tumors, with markedly different values found in necrotic cores (i.e., central regions of non-viable cells) than in actively proliferating outer rims and regions of infiltration [17, 37]. In addition, ADCs in regions of peritumoral edema may be higher than those of tumor boundaries, especially in cases of tumor metastases [17, 37].

Examination of the wide variations in ADCs of different regions of the brain demonstrates the necessity of describing diffusion rates for specific tissue subtypes and underscores the need for judicious selection of regions of interest in evaluation of brain ADCs. To further illustrate, diffusion rates of specific selected healthy and pathologic brain tissues are listed in Table 1.

Table 1: ADCs of selected healthy and cancerous brain tissues**.** The diffusion of water in healthy white matter is hindered by the presence of fiber tracts, yielding low ADCs in this tissue. Relatively low diffusion rates are also seen in malignant and cellularly dense tumors as compared to necrotic tissue, which is characterized by low cellularity. The ADCs of water-rich cerebrospinal fluid and cysts are comparable to that of pure water at body temperature (included for reference).

Tissue Description	**ADC** ($\times 10^{-3}$ mm^2/s)	**Reference**
Frontal White Matter	0.79	38, 39
Parietal White Matter	0.78	38
Deep Gray Matter	0.75	38
Parietal Gray Matter	0.85	39
Thalamus	0.85	39
Cerebellar Hemisphere	0.73	39
Cerebrospinal Fluid	2.9	39
Edematous Brain	1.3 - 1.4	17
Cyst	2.5 - 3.5	17, 19
Cellularly Dense Brain Tumor	0.60	17
Solid High-Grade Glioma	0.80 -1.3	17
Necrotic Glioma Core	1.8 - 2.4	17
Pure Water (Body Temperature)	3.0	17, 19

Matrix-assisted Laser Desorption Time-of-Flight Mass Spectrometry

The up-regulation of numerous proteins and peptides has been associated with tumorigenesis, especially those molecules involved in cellular proliferation, extracellular matrix degradation, and angiogenesis [40-43]. Matrix-assisted laser desorption ionization (MALDI) is a technique by which protein signatures may be identified and localized within intact *ex vivo* biological tissue specimens based on the molecular weight of the protein [44]. However, to uniquely specify individual proteins, additional analytical methods such as time-of-flight (TOF) mass spectrometry (MS) are often employed to yield information which supplements the molecular weights reported by MALDI [45-47]. MALDI methods are sensitive to proteins with masses ranging from 2 – 70 kDa [44, 45]

(note that peptides and proteins in murine tissues most often fall within the range of 2 – 30 kDa [44]). The mass measurement accuracy of combined MALDI-TOF-MS ranges from 100 – 200 ppm and the molecular sensitivity is in the attomole to femtomole range [2].

MALDI-TOF-MS instrumentation functions to provide proteomic information principally by means of separating ions based on their charges and molecular masses [47]. Components of a MALDI-TOF mass spectrometer are depicted schematically in Figure 3. The specimen to be analyzed (preparation techniques described below) is placed in a vacuum chamber and kept at a positive potential, typically 20 kV [47]. Select sample regions are then struck by photons, most commonly produced by nitrogen lasers yielding 337.1 nm pulses which are maintained for a duration of three ns [47]. The laser pulses cause the proteins within the sample to ionize, desorb, and enter the gas phase [48].

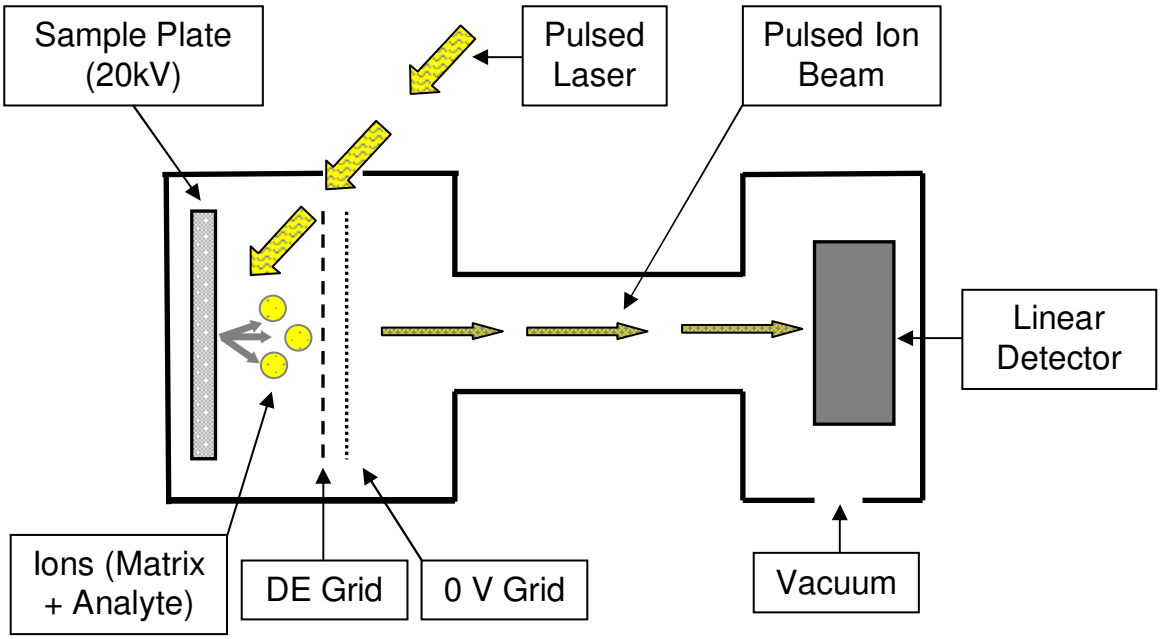

Figure 3: Schematic diagram of a linear MALDI-TOF mass spectrometer. The sample is held at an electric potential. Charged molecules are desorbed from the sample by impinging photons from a pulsed laser. Subsequent to being held briefly in a free-field region, the ions are accelerated down a flight tube towards a detector which records the number and arrival time of the ions. The entire system is held in vacuum.

In modern mass spectrometers, a delayed extraction (DE) grid is employed to improve mass resolution [47]. The DE grid is held at a potential equivalent to that applied to the sample plate, thus restraining the ion plume in a free-field region for time periods on the order of hundreds of ns [47, 48]. During the delay period, most neutral, light molecules diffuse away from the relatively heavier molecules of interest, which in turn travel a mass-dependent distance between the sample and the grid [47]. Upon completion of the delay period, the DE grid voltage is abruptly reduced, yielding graded, pulsed acceleration of the (fixed kinetic energy) ions through a grounded grid, followed by their drift through a flight tube towards the detector [47, 48]. The time of flight initiation is marked by the time of laser pulse collision with the sample and duration of DE, whereas the flight end time is recorded by the detector [46, 47].

The mass to charge ratio of an ion may be readily calculated from the observed flight time. The potential energy, E_p, at which the sample plate is held is given by

$$E_p = zU, \qquad \textit{(Equation 9)}$$

where z is the charge of the ion and U is the voltage across the plate [49]. As the ions are desorbed, the potential energy is converted to a fixed kinetic energy, E_k, of

$$E_k = \frac{1}{2}mv^2, \qquad \textit{(Equation 10)}$$

where m is the ion mass and v is the ion velocity [49]. Since the velocity of the ions in the vacuum drift tube is constant, v may be expressed as $\frac{L}{t}$, where L is the length of the flight path and t is the total time of flight. The equivalence of potential and kinetic energies thus yields

$$zU = \frac{1}{2}m\left(\frac{L}{t}\right)^2. \qquad \textit{(Equation 11)}$$

Rearrangement of Equation 12 clarifies that the ion mass to charge ratio and flight time are related *via* known constants, U and L, by

$$\frac{m}{z} = \frac{2t^2U}{L^2}. \qquad \textit{(Equation 12)}$$

Using this relationship, the record of the number of ions striking the detector is converted to spectra corresponding to mass to charge ratios and their relative intensities (peak amplitudes) [48].

To assure detailed and accurate measurements, strict adherence to careful specimen preparation procedures is necessary when undertaking MALDI experiments. Since albumin, immunoglobulins, and other high-abundance proteins may comprise more

than 90% of plasma and serum protein mass, exsanguination of animal subjects is often performed to prevent blood protein signatures from dominating MALDI signals from low-abundance proteins [5, 50, 51]. The exsanguination process involves removal of blood from the animal by saline perfusion *via* cardiac puncture, after which the tissue of interest is typically rapidly frozen to inhibit protein degradation. Tissue specimens are then sliced into sections using a surgical blade, microtome, or cryostat, to achieve slice thicknesses on the order of tens of microns [5, 52].

Tissue specimens are then further prepared for MALDI analysis by the application of a matrix compound such as that shown in Figure 4 [45, 46].

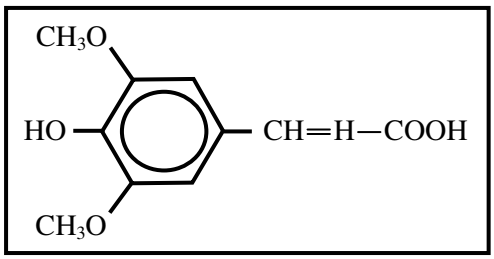

Figure 4: Chemical structure of sinapinic acid, a commonly used MALDI matrix for analysis of proteins [47]. The acidic matrix, MH^+, is applied to a sample, S, with which it cocrystallizes. Within the mass spectrometer, photons emitted by the pulsed laser strike the specimen, ionizing the sample as protons, H^+, are contributed by the matrix to the sample according to the reaction: $MH^+ + S \rightarrow M + SH^+$. The ionized sample molecules are then analyzed *via* TOF techniques in order to determine their mass to charge ratios.

MALDI matrices serve several functions, including cocrystallization of extracted analyte (i.e., macromolecules within the tissue specimen) over the surface of the specimen, protection of analyte structure by absorption of the energy of applied laser pulses, and ionization of the analyte molecules *via* contribution of one or more protons or electrons from the matrix to the analyte, depending on the relative pH between the matrix and the analyte [45-47].

Data Analysis

MALDI data collected during the course of this project will be examined using principal component analysis (PCA), a data-driven multivariate statistical technique that requires minimal *a priori* assumptions regarding latent variables [53]. In addition to its application in mass spectrometry [53], PCA has found use in a variety of fields, including image processing and compression, immunology, molecular dynamics, information retrieval, and others [54].

Several features of PCA contribute to its widespread success as an analysis method. For example, PCA techniques are able to detect weak signals in data, which is useful in denoising [53] and offers the potential to overcome limitations inherent to cluster analysis [54]. Furthermore, dimensionality reduction with little loss of information may be achieved using PCA by focusing analysis on only the most dominant data components (i.e., those which exhibit the highest degrees of variance) [53, 54]. These characteristics of PCA render it a powerful method for unbiased exploration of those protein signatures and diffusion measurements which share a common spatial distribution.

To begin PCA of MALDI data, a matrix M of dimension $n \times p$ is constructed in which n is the number of voxels sampled by MALDI and p is the number of discrete MALDI peaks at each voxel location The mean energy, $\overline{ms}$, of M is calculated as

$$\overline{ms} = \frac{\sum_{i=1}^{i=n} ms_i}{n} \qquad \textit{(Equation13)}$$

where ms_i is the MALDI mass spectrum measurements of the i^{th} imaging voxel. To decrease the effects of noise and reduce the number of MALDI peaks to a

computationally efficient number (e.g., from approximately tens of thousands to several hundred), an energy threshold may be set, below which all values are omitted from analysis.

A MALDI covariance matrix is then constructed and decomposed *via* singular value decomposition. Multiplication of each eigenvector by the original MALDI data generates a linear combination of eigenimages in which the entire MALDI dataset, M , is represented by

$$M = \sum_{j=1}^{j=\#images} \alpha_j E_j \,, \qquad \textit{(Equation14)}$$

where α_j is the j^{th} eigenvalue (i.e., weighting factor), and E_j is the j^{th} eigenimage. Each eigenimage then represents the relative concentration of MALDI data in space (i.e., how well the eigenvalue corresponds to a point in space). Thus, the application of PCA will permit examination of the contributions of independent eigenimages to correlations between ADC and proteomic metrics.

To examine the relationship between ADC and protein mass to charge ratios, the Pearson correlation coefficient, *r*, between each eigenimage and the ADC values in selected regions of interest (ROIs) will be calculated as

$$r = \frac{\sum_{i=1}^{i=n} (X_i - \overline{X})(Y_i - \overline{Y})}{\sum_{i=1}^{i=n} (X_i - \overline{X})^2 \sum_{i=1}^{i=n} (Y_i - \overline{Y})^2}, \qquad \textit{(Equation 15)}$$

where X_i and Y_i are the i^{th} ADC and eigenimage intensity measurements, respectively, and $\overline{X}$ and $\overline{Y}$ are the mean values of all ADC and eigenimage intensity measurements,

respectively [55, 56]. The significance of each correlation will be expressed using traditional *p*-value representation.

Methods

Animal Model

Animal procedures were approved by Vanderbilt University's Institutional Care and Use Committee. Two Wistar rats with an average mass of 250 g were anesthetized with a 2%/98% isofluorane/oxygen mixture. The rats were then injected with 1×10^5 C6 glioblastoma cells using a 10-mL gastight syringe approximately one mm anterior and two mm lateral to the bregma on the right side of the head, at a depth of three mm relative to the dural surface. Intracranial tumors emerged in one of the rats while one rat was found to develop only inflammation due to the needle insult. The latter rat was then selected to be used as a control. 15-16 days post-injection, the rats were anesthetized with a 2%/98% isofluorane/oxygen mixture and diffusion-weighted MR imaging was performed as described below.

MRI Protocol

MR data were acquired on a 9.4 T Varian DirectDrive scanner equipped with a 38 mm Litz coil and an in-house constructed rat restraint device to minimize motion. TR and TE values were 2000 and 25.56 ms, respectively. Diffusion gradient duration, δ, of 6 ms and spacing, Δ, of 15 ms, were used with amplitudes of 0, 6.31, and 9.98 mT/m, to yield *b*-values of 0, 400, and 800 s/mm^2. Data were collected in 128 $\times$ 96 matrices

spanning a 38.4 × 28.8 mm FOV achieving an in-plane resolution of 300 × 225 μm. The slice thickness was 0.5 mm with no gap between slices. Six image acquisitions were averaged for each rat.

The MR data was then imported into Matlab for analysis. Diffusion maps were generated for each slice of the two rat datasets using an in-house developed program which implemented linear regression analysis described by Equation 8. A selected diffusion map and the MR data from which it was generated are shown in Figure 5.

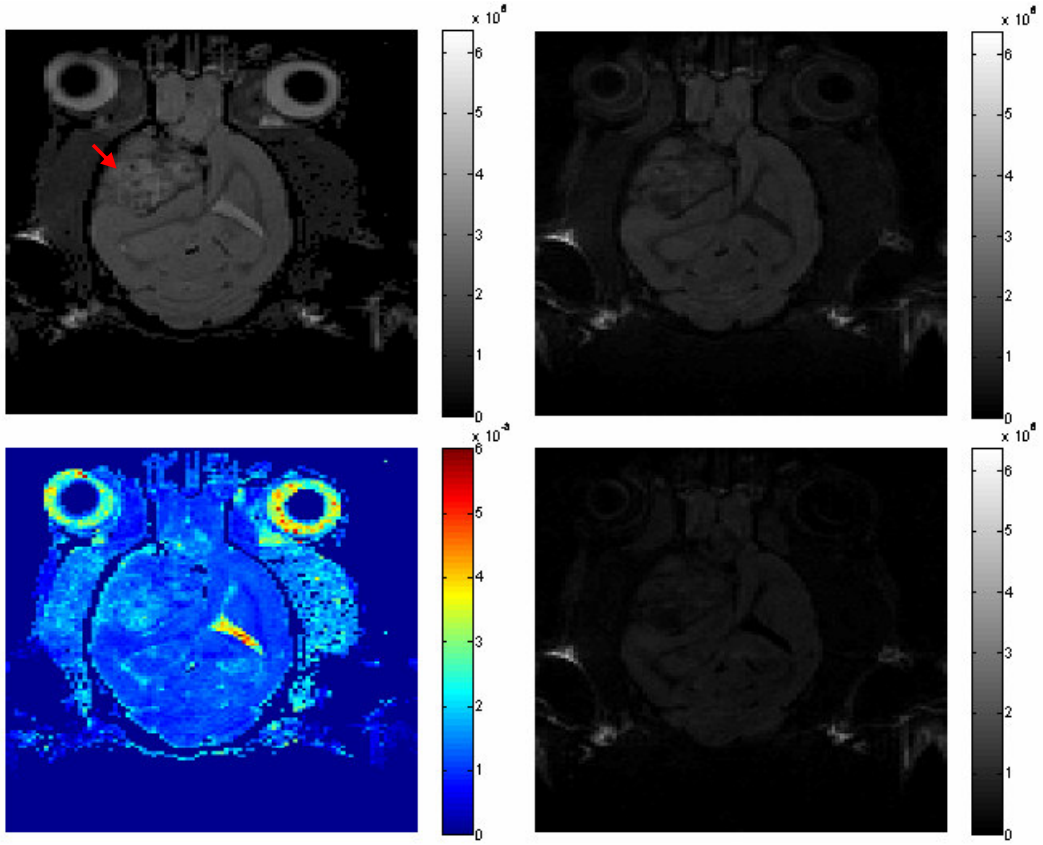

Figure 5: Diffusion-weighted MR images and ADC map for central slice of the tumor rat dataset. Clockwise from top left: MR images acquired with *b*-values of 0, 400, and 800 s/mm^2, respectively (units: arbitrary MR signal intensity), and the corresponding ADC map (units: mm^2/s). The location of the glioma is indicated by the red arrow (top left) and is visible in all three MR images as a relatively large, asymmetric region of heterogeneous signal intensity. The MR signal intensities of the three images are depicted on the same scale. Note the overall decrease in signal intensity as *b*-values are increased. The glioma is also observable as a region of variable diffusion rates in the ADC map. The largest ADC values appear in regions that have limited barriers to diffusion (see, e.g., the eyes and right ventricle).

MALDI Imaging Procedures

Immediately after *in vivo* MR data acquisition, a deep level of anesthesia was induced in each rat. The rats were then sacrificed *via* exsanguination and decapitated. The heads were flash-frozen in a hexane and dry ice solution and subsequently placed in a water bath which was frozen at -20º C until the time of the sectioning procedure. The

frozen rat heads were sectioned (Leica CM3600 Cryomacrotome) into 15 µm slices, with a mounted high resolution digital Canon camera system used to photograph every other slice for registration purposes (described below).

Specimen slices were placed on indium-tin-oxide coated glass plates and spotted with a MALDI matrix solution of 20 mg/mL sinapinic acid prepared in 50% acetonitrile and 0.1% trifluoroacetic acid. Ion images were acquired with 200 µm lateral resolution using a linear MALDI time-of-flight mass spectrometer (Autoflex III, Bruker Daltonics) equipped with a Smartbeam™ solid state Nd:YAG (i.e., neodymium-doped yttrium aluminium garnet) laser with an emission wavelength of 355 nm operating at 200 Hz. Each pixel was represented by the accumulation of 200 laser shots arranged in four different positions with a shot diameter of 150 microns as depicted in Figure 6. Mass spectra were collected for molecules with mass to charge ratios within the range of 2 to 40 kDa/charge.

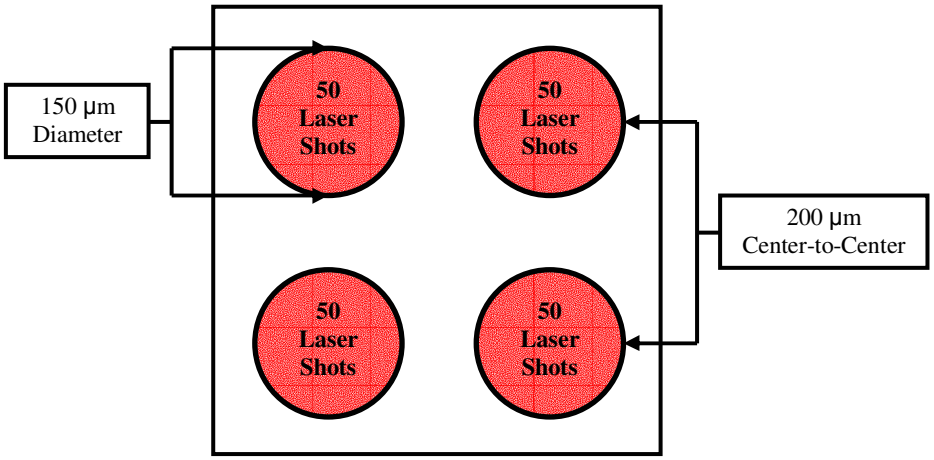

Figure 6: Arrangement of 200 MALDI laser shots in a single pixel. Four different positions in each pixel received 50 laser shots. The diameter of each laser shot was 150 µm and the center-to-center distance between the shot positions was 200 µm.

Coregistration of MR and MALDI Datasets

Using Matlab applications developed by the Center for Image Analysis of the Vanderbilt University Institute of Imaging Science, coregistered MALDI/ADC datasets were created for three slices each of control and tumor rat data, for a total of six datasets. The registration process relied on a three-dimensional (3D) digital construct, termed the "blockface", which served as an intermediate reference structure to which the MR and MALDI data were aligned to produce a registered multi-modal data set [5]. The blockface was comprised of the set of digital photographs of the rat heads obtained during sectioning of the specimens. The blockface volume was generated by an iterative alignment process in which each photograph was registered to the previous one using an intensity based algorithm based on normalized mutual information (NMI).[1]

The control rat blockface volume contained 450 photographs acquired at intervals of 30 µm to yield a total depth through the rat head of 13.53 mm (see Figure 7). The total depth represented in the blockface volume for the tumor rat was 22.89 mm (763 photographs). The estimated random error in depth assessment was 100 µm.

[1] NMI optimizes the similarity between two images by translation and in-plane rotation of the registration image to the target image to achieve a minimum in the NMI metric, joint entropy [57].

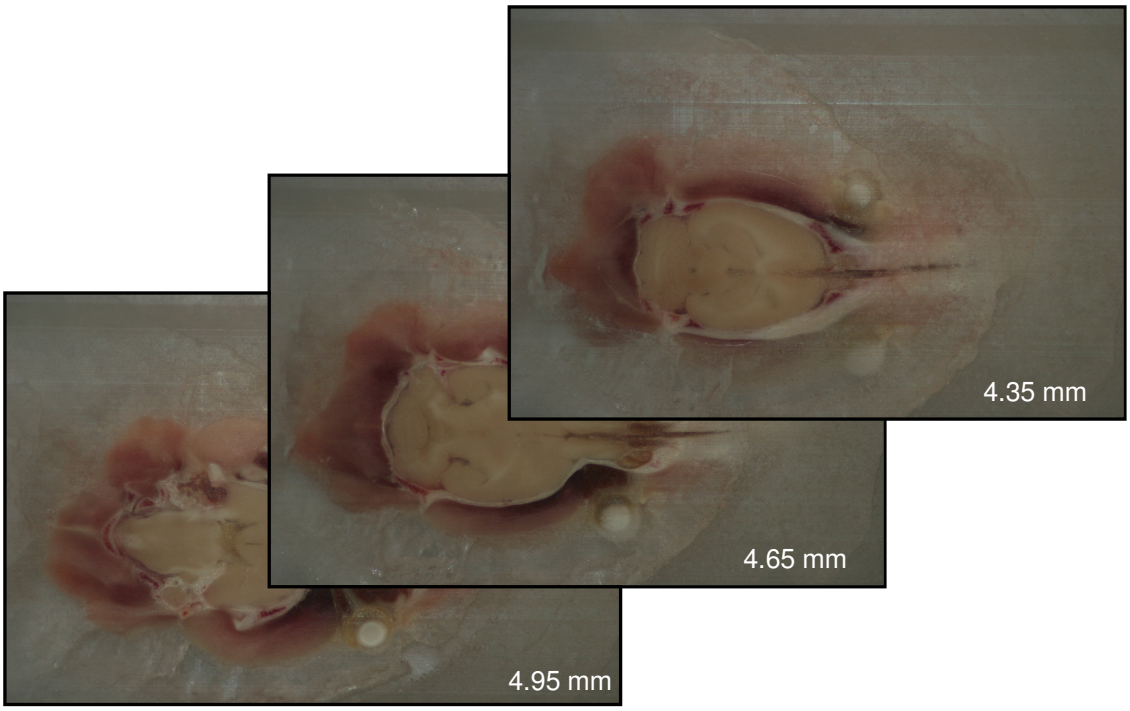

Figure 7: Subset of control rat blockface data. Three out of 450 photographs are shown with the slice depth relative to bregma indicated in the lower right corners of the images.

The two-dimensional locations within the tissue from which spectra were acquired were reported by the spectrometer during specimen analysis, thus intrinsically associating the MALDI with the corresponding tissue locations in the 3D blockface. Finally, the blockface data were registered to the MRI dataset using a six degree-of-freedom rigid body (with the skull as a stereotaxic frame) NMI-based technique. Due to lower resolution of MR data relative to MALDI data, ADC values which were missing for points in space corresponding to the MALDI measurements were interpolated using nearest neighbor methods.

Correlation Analysis

Application of PCA with a 1% energy threshold reduced the number of MALDI peaks from approximately 20,000 to 500. A 500 × 500 covariance matrix of the MALDI data was generated and decomposed *via* SVD. Each eigenvector was multiplied by the original MALDI data to yield a linear combination of 20 eigenimages.

In each of the six datasets, regions of interest (ROIs) within selected anatomical structures were manually delineated using in-house developed Matlab code. Anatomical features in the control rat were somewhat difficult to observe in the diffusion-weighted MR values translated into MALDI space. Thus, only two ROIs (those in the rat eyes) were delineated in the ADC data in MALDI space. The selection of an additional 25 ROIs was based on visual inspection of T_1-weighted MR data from the same rats (obtained during the same MR sessions for use in a separate study), which were also coregistered with the MALDI data. The ROI coordinates for the eyes in the ADC data and the 25 other ROIs from the T_1-weighted data were concatenated to yield three-dimensional data coordinates specifying the locations of a total of 27 ROIs in the first slice of control rat data. ROIs in T_1-weighted data for the first control slice are shown in Figure 8.

In the control rat, a total of 75 ROIs which corresponded to similar inter-slice structures were selected for correlation analysis. In each of the first and second slices, 27 ROIs were defined within apparently contiguous structures, while only 21 of the regions were present in the third (deepest, relative to bregma) slice. For example, ROIs were

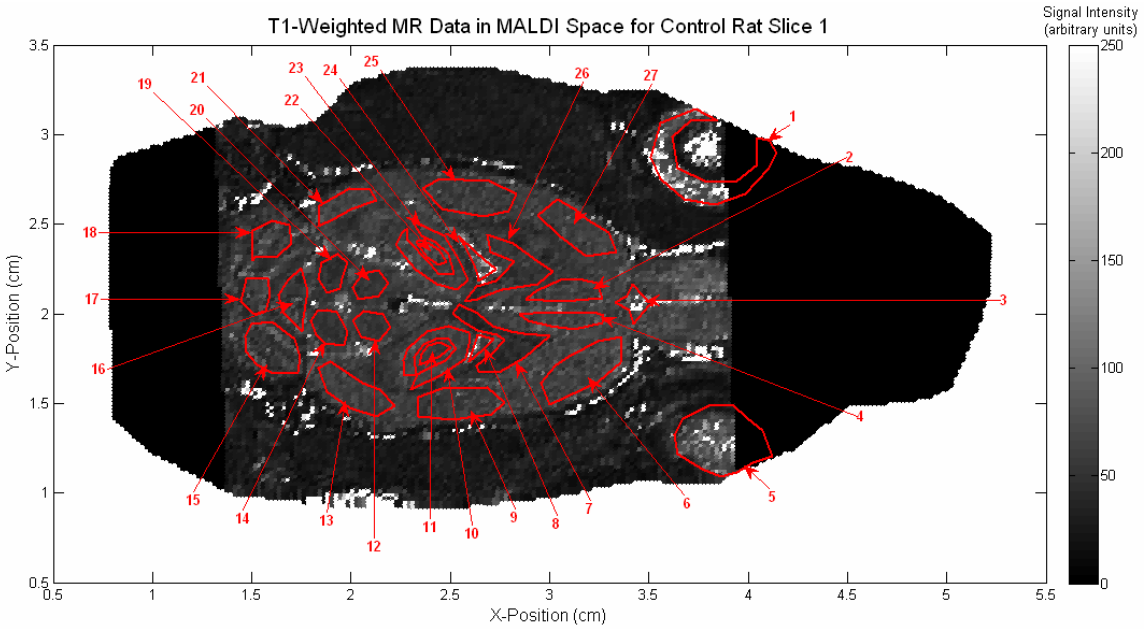

Figure 8: ROIs in T_1 data translated into MALDI space for control rat slice one. ROIs in ADC values in MALDI space were identified in each rat eye (ROIs 1 and 5).The T_1 data were used for manual identification of most ROIs (25 of 27), due to the ease of observation of anatomical features in T_1-weighted MR data. The two sets of ROI coordinates were concatenated after selection within the two MR datasets.

delineated within the dentate gyrus, lateral ventricles, and portions of the hippocampus in slices one and two. However, these structures were not visible at the depth of the third slice. Thus, each of these structures was omitted from analysis in the third slice, causing six contralateral ROIs to be absent from the third slice which were present in the first two. Figures depicting the ROIs for each of the control slices in the ADC data are included as Figures 16 – 18 in the Additional Figures section. The anatomical structures corresponding to each ROI in the control rat data are listed in Table 2 [58].

Table 2: Anatomical structures selected as ROIs within the control rat data.

Anatomical Structure	ROI Number(s)
Eyes	1, 5
cingulate cortex	2, 4
rhinal incisura	3
cortex, rostrolateral	6, 27
caudate putamen	7, 26
lateral ventricle	8, 24
cortex, mediolateral	9, 25
Hippocampus	10, 23
dentate gyrus	11, 22
superior colliculus	12, 20
cortex, posteriolateral	13, 21
inferior colliculus	14, 20
Cerebellum, lateral	15, 18
Cerebellum, medioanterior	16
Cerebellum, medioposterior	17

Anatomical features were obscured to a greater extent in the tumor rat than in the control rat due to variations in the orientation of the rat head during MR imaging and MALDI sectioning. Furthermore, diagonal "streaks" were observed in each slice of the tumor ADC data translated into MALDI space. These visual phenomena were presumably caused by distribution of the dynamic tumor MR data across the MALDI imaging plane. Nevertheless, the tumor rat data permitted selection of 29 ROIs corresponding to 13 inter-slice regions of similar feature, if not actual anatomical structure. The ROIs in ADC data for the first tumor slice are shown in Figure 9, while those for the second and third are included as Figures 19 and 20 in the Additional Figures section. The anatomical regions corresponding to each ROI in the tumor rat data are listed in Table 3 [58].

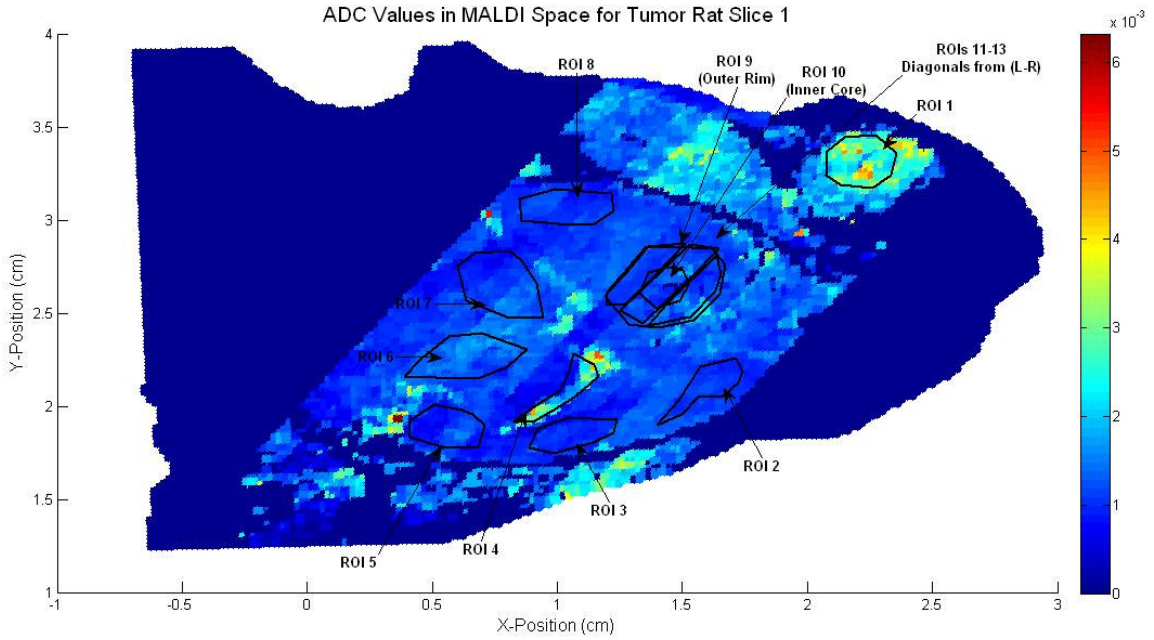

Figure 9: ROIs in ADC data translated into MALDI space for tumor rat slice one. Data quality reflects misalignment of the rat head during MR imaging and MALDI sectioning, as well as the distribution of dynamic MR data across the resolution of the MR scanner.

Table 3: Anatomical regions selected as ROIs within the tumor rat data.

Anatomical Region	ROI Number(s)
left eye	1
cortex, rostrolateral	2
cortex, mediolateral	3, 8
right lateral ventricle	4
cortex, posteriolateral	5
hippocampus, right	6
dentate gyrus, left	7
tumor outer rim	9
tumor core	10
tumor, left diagonal ROI	11
tumor, medial diagonal ROI	12
tumor, right diagonal ROI	13

For each rat, the correlations between ADCs and eigenimage intensities in each ROI were calculated on a voxel-by-voxel basis using the Pearson correlation coefficient,

r, and p-value significance ratings. Also for each rat, two-sample t-tests were conducted to determine the statistical equivalence, or lack thereof, between the ADC populations of both intra- and inter-slice ROIs. ADC similarities were not compared between the two rats.

Separately in each of the rats, ROIs within contiguous inter-slice anatomical regions which featured similar ADCs while concurrently exhibiting dissimilar intra-slice ADCs were selected for further analysis. For example, relatively high ADCs were present in the rhinal incisura of all slices, as compared to lower ADCs observed during intra-slice comparisons between the rhinal incisura and the cerebellum. Specific eigenimages which correlated significantly with these ROIs' ADCs were compared in order to examine the theory that, within a given tissue type, equivalent ADCs may be correlated with identical protein signatures. For the results which were consistent with this theory, the eigenspectra used to generate the eigenimages that correlated with the selected ROIs' ADCs were inspected for the presence of specific mass to charge ratios which exhibited high-amplitude spectral intensities in each slice's eigenspectrum. A literature search was then conducted to identify possible proteins represented by these values of mass to charge ratios.

Results and Discussion

Overall Correlations between ADC and Eigenimages

The linear Pearson correlation coefficient, *r*, and associated p-values were calculated between the ADC values of each voxel within each ROI and each of 20

eigenimages for a total of 75 ROIs representing 27 anatomical structures in the control rat and 39 ROIs corresponding to 13 different anatomical regions in the tumor rat. The correlations were classified as statistically significant when their associated p-values were ≤ 0.05. As summarized in Figure 11, significant correlations were identified in 44.0% (41.2% of control; 49.4% of tumor) of all calculations of correlations between ADC and eigenimage intensity in all ROIs. For the correlations between ADC and eigenimages which were deemed significant, the mean *r*-value for the control rat was 0.348 ± 0.137. For the significant correlations of the tumor rat, the mean *r*-value was 0.331 ± 0.122. Since the eigenimages represent the relative concentration of MALDI data at each image point, these results are consistent with the theory that diffusion measurements reported by MR correlate spatially with protein signatures obtained *via* MALDI methods.

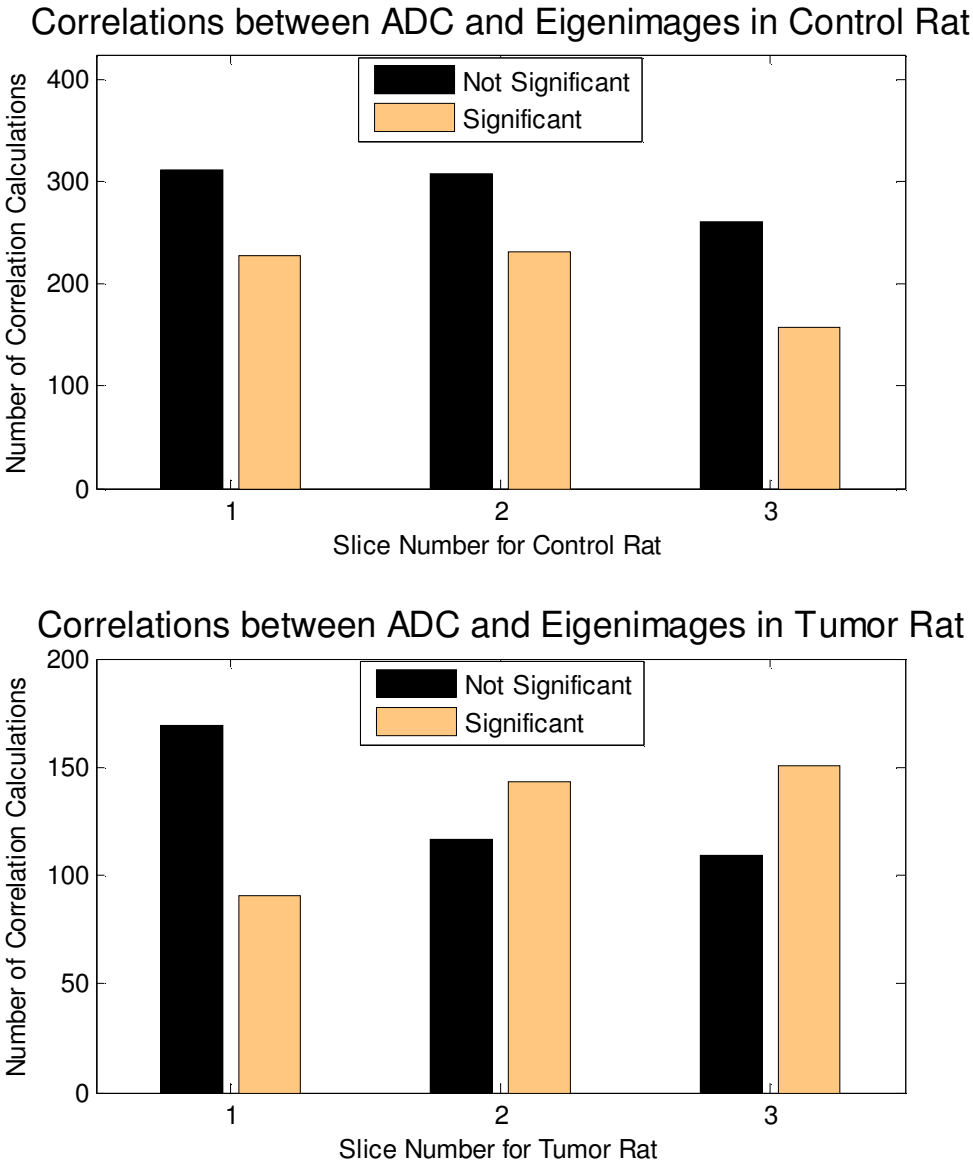

Figure 10: Correlations between ADC and eigenimages for each slice of control and tumor rat data. Correlations were classified as statistically significant when their associated p-values were ≤ 0.05. Significant correlations were found between the two metrics in a total of 44.0% of calculations for both rats

Correlations between ADC and Selected Eigenimages

The results described above show that ADC and eigenimage intensities within selected anatomical regions of healthy and tumorous rat brains correlated in 44.0% of

comparisons between 114 ROIs and 20 eigenimages. In order to examine the correlation between *specific* ADC populations and *individual* protein signatures, subsets of ROIs within the control and tumor rat data were selected for further analysis. The ROIs included in these subgroups exhibited two features: (1) ADC values in the ROI were statistically similar at each depth (slice) in the rat head and (2) ADC values in the ROI were statistically different from those of other ROIs in the same slice which were chosen for further examination.

In the control rat, three ROIs were selected for further correlation analysis. The first ROI which was found to exhibit statistically similar ADC values in all three slices of control rat data (criterion (1) for continued analysis) was located in the rhinal incisura. The right superior colliculus was also characterized by statistically similar ADC values in all three slices of control rat data. In addition, the ADC values in the rhinal incisura and right superior colliculus differed statistically from one another within each slice (criterion (2) for continued analysis). The ADC populations in the right lateral cerebellum were similar in slices two and three, yet statistically different from the ADCs of this ROI in slice one, meeting criterion (1) for inclusion in 2/3 of the control rat dataset. The ADC populations of the right lateral cerebellum also differed from those of the rhinal incisura and right superior colliculus, fulfilling criterion (2) for continuing analysis. The relationships between ADCs in these three ROIs are summarized in Table 4. The t-statistic and p-values calculated during the two-sample t-tests used to generate Table 4 are shown as Tables 10 and 11 in the Additional Tables portion of the Appendix.

Table 4: Summary of control rat ADC T-test results in selected ROIs. Statistical difference (— = absent; ✓ = present) of ADC populations is indicated for each slice and ROI comprising the control rat data subset used for continued analysis. Within each slice, the ADCs of the rhinal incisura, right superior colliculus, and right lateral cerebellum are statistically dissimilar, while each ROIs' ADC values are statistically equivalent across slices. The mean and standard deviation of the ADC values in each ROI are included for reference.

	ROI	Rhinal Incisura			Sup. Colliculus			Cerebellum	
	Slice	1	2	3	1	2	3	2	3
Mean ADC ($x10^{-3}$ mm^2/s)	$1.5 \pm 6x10^{-4}$	—	—	—	✓	✓	✓	✓	✓
	$1.1 \pm 2x10^{-4}$	✓	✓	✓	—	—	—	✓	✓
	$0.9 \pm 2x10^{-4}$	✓	✓	✓	✓	✓	✓	—	—

Having identified control rat ROIs in which the ADCs were unique on an intra-slice basis but similar across slices, specific protein signatures which correlate with these diffusion trends are now sought. As suggested by the incidence of 41.2% significant correlation calculations in the control rat, many ROIs correlated with one or more eigenimages. For those ROIs in which statistically equivalent inter-slice diffusion rates correlated with more than one eigenimage, the eigenimage associated with the greatest mean inter-slice correlation was selected for continued spectral analysis. For example, in each slice of control rat data, the right superior colliculus exhibited statistically similar ADC values and correlated with multiple eigenimages, including eigenimages 7, 15, and 18. The mean correlations between ADC and eigenimage intensity in the right superior colliculus for eigenimages 7, 15, and 18 were 0.324, 0.324, and 0.338, respectively. Thus, eigenimage 18 was chosen for further analysis due to its relatively higher mean correlation with ADC in the right superior colliculus, while eigenimages 7 and 15 were excluded from further analysis associated with this ROI. Eigenimage 18 and the location of the right superior colliculus within it are shown in Figure 11. The subset of

eigenimages with which control rat ROIs in the rhinal incisura, right superior colliculus, and right lateral cerebellum correlated is described in Table 5.

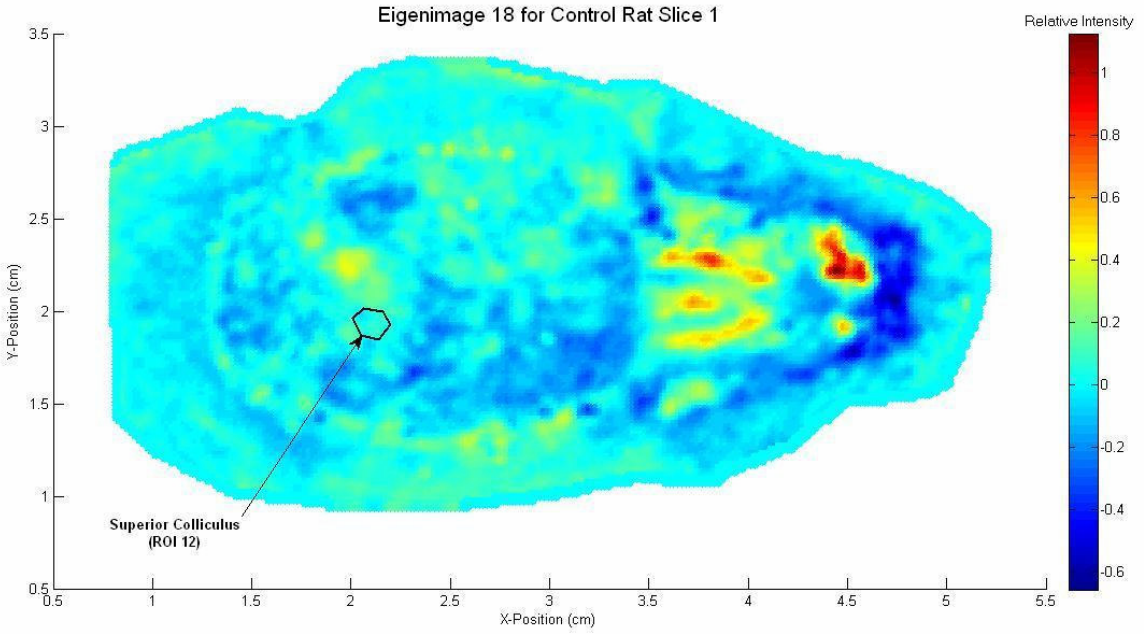

Figure 11: Eigenimage 18 for control rat slice one. The ADCs and eigenimage intensities correlated significantly (r_{mean} = 0.338) in the right lateral superior colliculus, which is identified in the figure as the ROI outlined in black.

Table 5: Control rat selected ROI correlations with three different eigenimages. For each slice and ROI, the eigenimage number, the Pearson correlation coefficient (r), and the associated p-values are given.

ROI	Rhinal Incisura			Superior Colliculus			Cerebellum	
Slice	**1**	**2**	**3**	**1**	**2**	**3**	**2**	**3**
Eigenimage	4	4	4	18	18	18	3	3
***r*-value**	0.532	0.414	0.548	0.333	0.288	0.395	0.487	0.206
p-value	0.000	0.026	0.010	0.016	0.026	0.004	0.000	0.007

Similarly to the control rat, three ROIs for the tumor rat were selected for further correlation analysis. The ROIs were located in the medio-lateral cortex, the general region of the right hippocampus, and the inner core of the tumor. However, ROIs which

exhibited statistically equivalent inter-slice ADC populations were observed in only the first and third slices. Thus, in order to maintain consistent methodology in processing the data from both rats, it was necessary to omit the second (middle) tumor rat slice from continued examination. All intra-slice ADC values for each ROI in the continuing analysis subset differed statistically from those of the other ROIs. The ADC t-test results are summarized in Table 6, with the corresponding t-statistic and p-values given as Tables 12 and 13 in the Additional Tables portion of the Appendix.

Table 6: Summary of tumor rat ADC T-test results. Statistical difference (— = absent; ✓ = present) of ADC populations is indicated for each slice and ROI comprising the tumor rat data subset used for continued analysis. Within each slice, the ADCs of the mediolateral cortex, hippocampus, and tumor core are statistically dissimilar, while each ROIs' ADC is statistically equivalent across slices. The mean and standard deviation of the ADC values in each ROI are included for reference.

	ROI	**Mediolateral Cortex**		**Hippocampus**		**Tumor Core**	
	Slice	**1**	**3**	**1**	**3**	**1**	**3**
Mean ADC ($x10^{-3}$ mm^2/s)	**$0.9 \pm 2x10^{-4}$**	—	—	✓	✓	✓	✓
	$1.4 \pm 2x10^{-4}$	✓	✓	—	—	✓	✓
	$1.1 \pm 3x10^{-4}$	✓	✓	✓	✓	—	—

As was found with the control rat, ROIs in the tumor rat often exhibited correlations with multiple eigenimages. Again as with the control rat, overlap was identified in the subset of eigenimages with which the selected ROIs correlated, as shown in Table 7. An example eigenimage of correlation is given in Figure 12, which was found to have a mean correlation of 0.330 with the ADC values in the voxels located within the central core of the tumor.

Table 7: Tumor rat selected ROI correlations with three different eigenimages. For each slice and ROI, the eigenimage number, the Pearson correlation coefficient (*r*), and the associated p-values are given.

ROI	Mediolateral Cortex		Hippocampus		Tumor Core	
Slice	**1**	**3**	**1**	**3**	**1**	**3**
Eigenimage #	18	18	1	1	2	2
***r*-value**	0.308	0.567	0.221	0.207	0.392	0.268
p-value	0.001	0.000	0.002	0.005	0.001	0.017

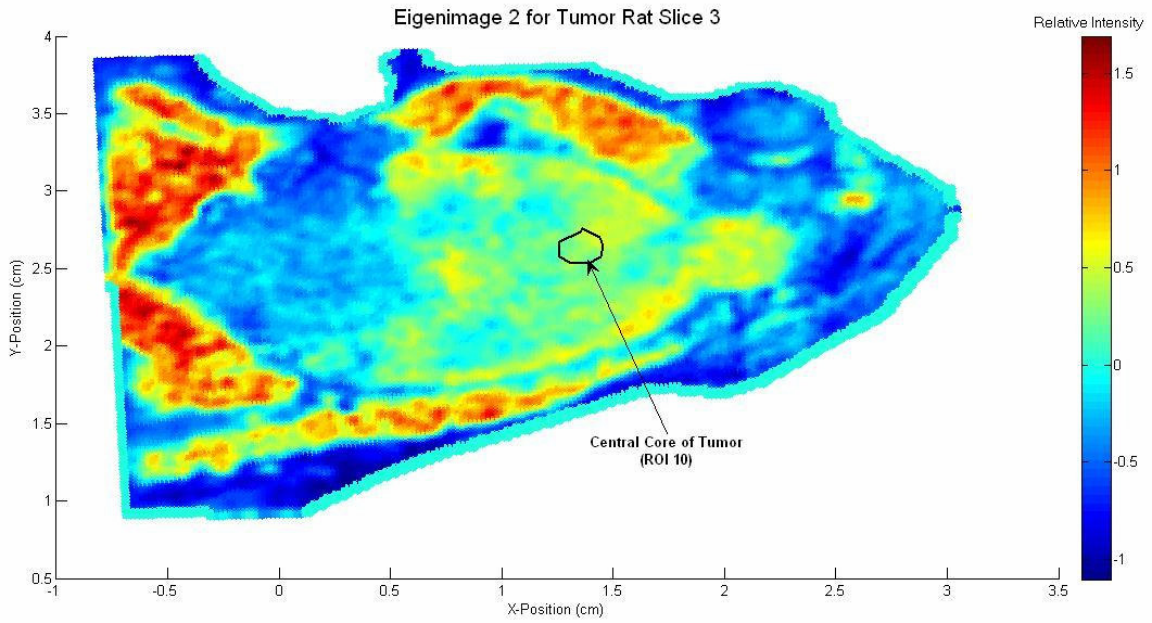

Figure 12: Eigenimage 2 for tumor rat slice three. The ADCs and eigenimage intensities correlated significantly (r_{mean} = 0.330) in the central core of the tumor, which is identified in the figure as the ROI outlined in black.

Selected Eigenspectra of Significant ADC Correlation

While each eigenimage represents the relative concentration of MALDI data in space, the corresponding eigenspectrum denotes which specific mass to charge ratios generate the peak amplitude intensities which give rise to variations in the eigenimage.

Thus, the eigenspectra of eigenimages which correlate with ADC populations in the above results are now inspected for protein identification.

Figure 13 plots the eigenspectra peak amplitude versus the mass to charge ratio for eigenspectrum 4, which correlates with ADC populations in the rhinal incisura, in each of the control rat slices. Although MALDI data was collected on the range of 2 – 40 kDa/charge, the sensitivity in the control rat data falls off rapidly beyond the 14 kDa/charge range (top panel). Examination of these independent eigenspectra on restricted ranges (bottom panels) yields the qualitative observation that the peaks are well-aligned, particularly in the 2 – 5 kDa/charge range (left bottom panel). Thus, not only do the same proteins (points in each plot) appear to be present in the tissue of the control rat in the rhinal incisura, but their concentrations vary quite similarly (peak rise and fall). The alignment of the peak location and amplitude decreases somewhat as the mass to charge ratio increases, which may reflect either or both of the following: variations in the presence and concentration of high molecular mass proteins and decreasing sensitivity. Plots of eigenspectra which correlate with control rat ROIs in the right superior colliculus and the right lateral cerebellum can be found as Figures 21 and 22 in the Additional Figures portion of the Appendix.

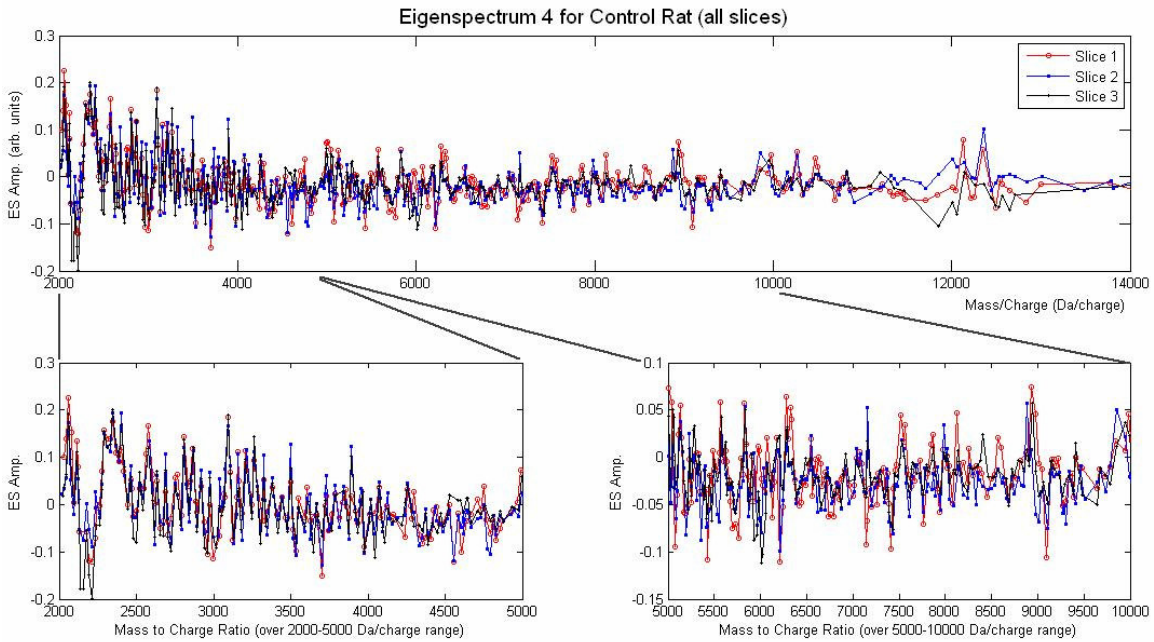

Figure13: Control rat eigenspectrum 4 for all three slices. The corresponding eigenimage correlated significantly with the rhinal incisura in the control rat data. The peaks in each slice's eigenspectrum appear qualitatively similar, especially for low mass to charge ratios, indicating the similarity of proteins as well as their concentrations in the rhinal incisura in each slice of the control rat data. The peaks spread apart both in amplitude and location as mass to charge ratio increases, implying somewhat greater variations in the presence of high-mass proteins in the rhinal incisura. Sensitivity falls off sharply beyond 14 kDa/charge.

Figure 14 plots the eigenspectra peak amplitude versus the mass to charge ratio for eigenspectrum 2 for tumor rat slices one and three. This eigenspectrum was found to correlate well with the ADCs of central tumor core in the two tumor rat slices. The sensitivity of MALDI data for the tumor rat data is much lower than that for the control rat beyond approximately 6 kDa/charge, with the signal disappearing entirely for tumor rat slice one at around 11 kDa/charge. Qualitatively, the peaks in this eigenspectrum are somewhat less well-aligned than those in the control rat eigenspectra. In the 2 – 4 kDa/charge range (left bottom panel), the location of the peaks are relatively well-matched between the eigenspectrum of the first and third slice. Furthermore, the peaks'

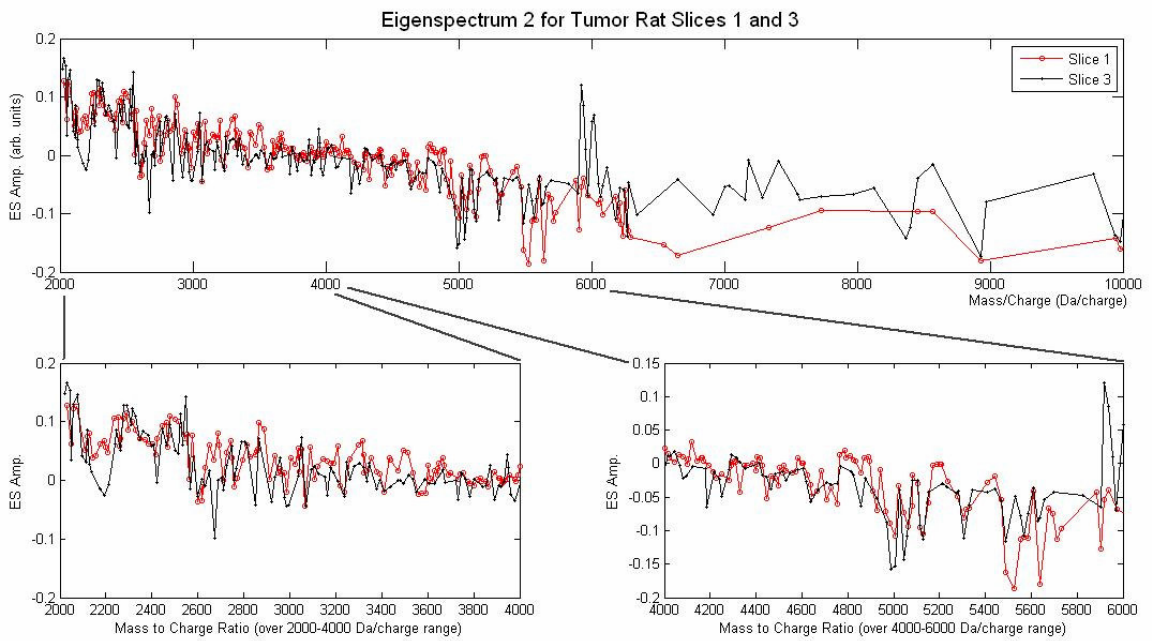

Figure 14: Tumor rat eigenspectrum 2 for slices one and three. The corresponding eigenimage correlated significantly with the central core of the tumor in the tumor rat data. Throughout the range of mass to charge ratios, the peaks in each slice's eigenspectrum frequently appear with moderately qualitatively similar amplitudes and locations, suggesting that multiple proteins of similar mass and concentration are present in both slices of the tumor data. Sensitivity of the tumor rat MALDI data falls off sharply beyond 11 kDa/charge.

amplitudes are at similar heights, indicating that the same low-mass proteins may be present in both slices, with relatively similar concentrations. The locations and amplitudes of the peaks differ increasingly as the mass to charge ratio increases, suggesting that the protein content of the two data slices varies increasingly for higher-mass proteins. Plots of eigenspectra which correlate with tumor rat ROIs in the region of the right hippocampus and the mediolateral cortex can be found as Figures 23 and 24 in the Additional Figures portion of the Appendix. The results of this portion of the study are consistent with the theory that similar ADC populations within specific tissue types correlate with eigenspectra characterized by qualitatively similar protein profiles and concentrations.

Identification of Protein Signatures in MALDI Spectra

To identify specific proteins which may be represented by the mass to charge ratios of the eigenspectra which correlate with ADC values in selected ROIs, it is first assumed that the most likely charge of the ionized protein is +1. Justification of this assumption is based upon consideration that an acidic matrix was used for analyte ionization and that the probability of MALDI formation of multiply charged ions decreases with molecular mass, becoming unlikely for low-mass (< 100 kDa) proteins such as those observed in this study [59].

The range of proteins selected for identification was limited on the low end (2 – 6 kDa) by the preponderance of low-mass peptides and fragmented protein subunits in this mass range. Within the higher range of molecular masses (> 13 kDa), identification of proteins was not attempted because of the low sensitivity of the MALDI data in this mass range. However, between the molecular mass range of 7.5 – 12.5 kDa, peaks were identified in eigenspectra of interest which correspond in the literature to six known proteins, with agreement at the mass resolution of 100 Da. The first such set of peaks is shown in Figure 15 in eigenspectra 4 of three data slices in the control rat at 7.5 kDa, representative of insulin-like growth factor II (IGF II) [60, 61]. The IGF II peak is isolated in the dark gray rectangle near other observed peaks at 7.6 kDa (to two significant digits).

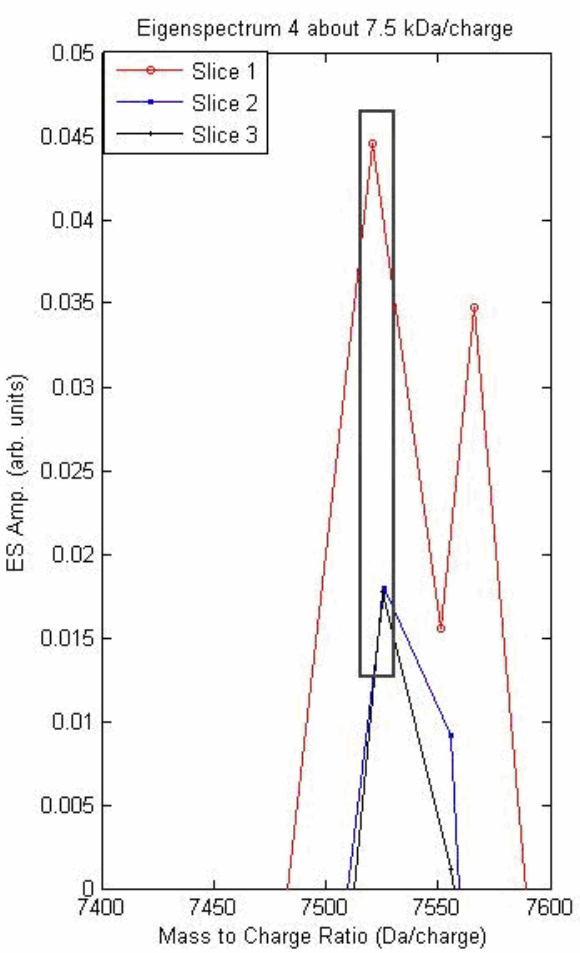

Figure 15: Eigenspectrum 4 from the 7.4 – 7.6 kDa range for all three slices in the control rat data. Peaks are observed in all three spectra about the 7.5 kDa/charge point (dark gray rectangle). Assuming a charge of +1, the mass to charge ratio represents the presence of IGF II. Also visible are peaks at ~ 7.6 kDa, which were not found in the literature.

Multiple peaks were present in the range of eigenspectra amplitudes targeted for investigation. However, a limited number of unambiguous peaks were chosen for ease of identification. In all, five other proteins including insulin-like growth factor I, ubiquitin, acyl-CoA binding protein (structurally identical to diazepam-binding inhibitor [62]), parvalbumin, and cytochrome c were identified in the same manner of visual inspection of peaks in eigenspectra of correlation with ADC. These proteins are described in Table 8.

Table 8: Description of six proteins identified in the control and tumor rat. These proteins were each found in eigenspectra of correlation with ADC in selected ROIs in the control and tumor rat.

Name	Abbr.	Mass (kDa)	Description	Source
Insulin-Like Growth Factor II	IGF II	7.5	supports neuronal growth and survival	60; 61
Insulin-Like Growth Factor I	IGF I	7.7	supports neuron, improves wound healing	63
Ubiquitin	—	8.5, 8.6	target proteins for degradation	64; 65
Acyl-CoA Binding Protein/ Diazepam-Binding Inhibitor	ACBP/DPI	9.9	binds fatty acids to proteins	62, 66
Parvalbumin	PARV	12.1	calcium binding protein, global second messenger	67
Cytochrome C	—	12.4, 12.5	involved in electron transport chain and apoptosis	68-70

Two of the proteins identified in the spectral data were each described in literature at more than one molecular mass. Specifically, ubiquitin is described as both an 8.5 and 8.6 kDa protein [65 and 64, respectively] while cytochrome c is found as both a 12.4 and 12.5 kDa protein [69 and 70, respectively]. For the former protein, peaks in eigenspectra of interest were identified at both masses in all sets of control and tumor rat data. For the latter, peaks were found in all three slices of the control rat data, whereas the low sensitivity of MALDI data for the tumor rat prohibited definitive assessment of the presence or lack of the protein. Similarly, the presence of parvalbumin could not be determined in the tumor rat data, while the protein was found in all slices of the control rat data. In contrast, IGF II was found in all slices of the control rat data and in slice three of the tumor rat data, but was absent in slice one of the tumor rat data. These findings are summarized in Table 9.

Table 9: Location of six proteins identified in the control and tumor rat. These proteins were identified in eigenspectra of significant correlation with ADC in selected ROIs of control and tumor rat data. The mass to charge ratio is assumed equal to the mass. The eigenspectra in which the proteins were identified can be located in the left column of the table. IGF II was identified in all slices of the control rat data and in slice 3 of the tumor rat data. IGF I, ubiquitin, and ACBP/DBI were found in all data. Parvalbumin and cytochrome c were present in the control rat data but assessment of their presence in the tumor rat dat was precluded by low MALDI sensitivity in the >12 kDa mass range. (Abbreviations: ES = Eigenspectrum; C = Control rat; T = Tumor rat; Y = yes for all slices; S3 = slice 3).

	Mass (kDa)	**7.5**	**7.7**	**8.5 and 8.6**	**9.9**	**12.1**	**12.4 and 12.5**
	Protein	**IGF II**	**IGF 1**	**Ubiquitin**	**ACBP/ DBI**	**PARV**	**Cytochrome C**
Data Location	C - ES 4 rhinal incisura	Y	Y	Y	Y	Y	Y
	C - ES 18 superior colliculus	Y	Y	Y	Y	Y	Y
	C - ES 3 cerebellum	Y	Y	Y	Y	Y	Y
	T - ES 18 cortex	S3	Y	Y	Y	N/A	N/A
	T - ES 1 hippocampus	S3	Y	Y	Y	N/A	N/A
	T - ES 2 tumor core	S3	Y	Y	Y	N/A	N/A

While this portion of the analysis has identified several proteins which may give rise to correlations between ADC values and low molecular mass protein signatures in both healthy and tumorous rat brain tissues, these results are unable to address the correlations that may exist between ADC populations and higher molecular mass proteins, due to the insensitivity of the collected MALDI data beyond the mass range of approximately 12.5 kDa/charge. However, the results described herein demonstrate a novel technique for identification of correlations between non-invasive MR measurements and their underlying molecular-level contrast sources.

CHAPTER II

CONCLUSIONS

While the results of this study have yielded initial support for the theory that molecular-level proteomic expression correlates with contrast in diffusion-weighted MR data, they have also exposed some of the underlying difficulties inherent to analysis of hybrid data. Technical complications arose during data acquisition, including loss of coregistered MR and MALDI tumor rat data due to misalignment of the head during sectioning. This factor confounded accurate delineation of ROIs corresponding to specific anatomical structures in the tumor rat, thus complicating quantification techniques. Moreover, ADC artifacts observed in the tumor rat MR data further draw into question the source of results in correlation calculations, since the heterogeneous "streaks" in the data make it difficult to localize ADC variations.

While MALDI techniques have been gaining both favor and technological advancements in recent decades, several obstacles have yet to be overcome in the methods. For example, identification of specific proteins in spectral data is hindered by proteomic processes including phosphorylation, dimerization, and fragmentation. Furthermore, the lack of ability to discriminate the exact charge transferred by the matrix to the analyte constitutes an additional problem. While the latter factor most probably did not impact the results of this study, owing to the low molecular masses involved (and their consequent unlikelihood of being multiply charged during ionization), acquisition of

MALDI data over a wider range of mass to charge ratios suffers to a greater extent from this limitation.

This study used fewer subjects than many cohort studies, suggesting an inability to assess repeatability. However, it should be noted that each mass spectrum in each pixel in each data slice constituted an independent measurement, thus generating a large volume (~ 10^6 measurements) of data. Hence, the observation of repeated eigenspectra peaks and amplitudes at specific mass to charge ratios in different data sets offers some insight into the repeatability of results described herein.

The objective of this thesis was to elucidate the molecular-level influences on ADC variations in a C6 rat glioma model of brain cancer. The results obtained during the course of this project suggest that proteomic profiles exert a substantial influence on diffusion metrics. However, this study constitutes only an early step towards the overarching goal of improving clinical cancer care by using non-invasive methods to monitor cellular-level tumor status. Future studies to verify and expand upon these preliminary findings are necessary to determine the feasibility of these techniques for large-scale studies.

Future work should incorporate several variations from the methodology of this study. First, additional care should be taken during the sectioning procedures in order to achieve higher-quality specimen slices for MALDI data acquisition. Several MR imaging parameters may be modified to increase resolution and signal-to-noise ratio, including decreasing the slice width and increasing the number of image acquisitions averaged for each rat. Similarly, decreasing the operating frequency of the MALDI laser and the matrix spot diameter and gap would increase data quality. Furthermore, the range

of mass to charge ratios at which proteomic metrics are collected should be expanded to 70 kDa/charge, as many proteins generally upregulated in cancer and specifically overexpressed in the C6 line have molecular masses well above 40 kDa (e.g., activated matrix metalloproteinase-2 ~ 62 kDa [71]; poly(ADP-ribose) glycohydrolase ~ 53 - 85 kD [72]; and vascular endothelial growth factor ~ 45 kDa [73, 74]).

Future research would also benefit by a change in several study parameters. Consider a study using the techniques described in this thesis and the imaging parameters described above in which six rats were used as follows: two control, two in which a C6 model of brain cancer was implemented, and two in which the RG2 model of brain cancer was implemented. While the data acquisition time and the volume of data generated would both be increased substantially, the study would offer the opportunity to investigate several important questions. First, the project would provide validation of or refute the correlations found in this work between ADC and protein signatures. Secondly, the increase in data resolution and the use of two different cell lines would provide the information necessary to examine whether there might exist not only a correlation between ADC and protein expression, but a correlation between *patterns* in ADC and protein expression. Identification of trends in the two metrics or their differentials would begin to address the feasibility of the clinical use of diffusion-weighted MR as a proxy for latent molecular-level proteomic information.

In summary, this study examined ADC and MALDI data which were acquired for a control rat and a rat in which C6 glioma cells were implanted. Principal component analysis was applied to the MALDI data to yield a set of 20 independent eigenimages, each voxel of which represented the relative concentration of MALDI data at a specific

spatial location. The ADC values and eigenimage intensities were compared within 114 selected anatomical regions using the linear Pearson correlation coefficient. The two data sets correlated significantly (p-value $\leq$ 0.05) in 44.0% of the comparisons. Six ROIs (three in the control rat data and three in the tumor rat data) were identified which exhibited statistically dissimilar ADC values when compared with those of the other ROIs on an intra-slice basis while concurrently exhibiting statistically equivalent values at each depth within the rat head. Eigenimages which correlated with the ADC populations in these ROIs were used to identify eigenspectra to be examined for the presence of specific protein signatures. It was found that similar ADC populations within specific tissue types correlate with eigenspectra characterized by qualitatively similar protein profiles and concentrations. Six low-mass proteins (IGF I and II, ubiquitin, ACBP/DPI, parvalbumin, and cytochrome c) were identified in the eigenspectra which correlated with ADC measurements in selected anatomical regions within the control and tumor rat. Signatures of proteins having masses greater than approximately 13 kDa could not be identified in the eigenspectra, due to low sensitivity to higher-mass proteins during the MALDI data acquisition process. The methods developed in this study constitute a novel approach for identification of correlations between non-invasive MR measurements and their underlying molecular-level contrast sources.

APPENDIX

A. ADDITIONAL FIGURES

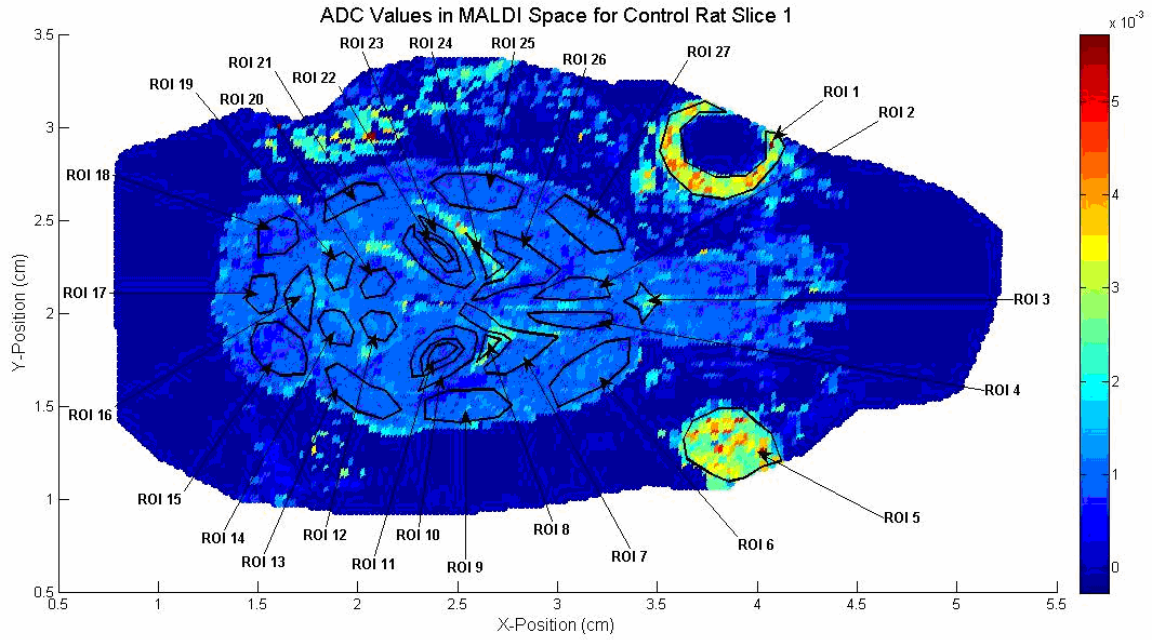

Figure 16: ROIs in ADC data translated into MALDI space for control rat slice one. The ROIs are numbered such that anatomical structures across slices are identified by identical ROI numbers.

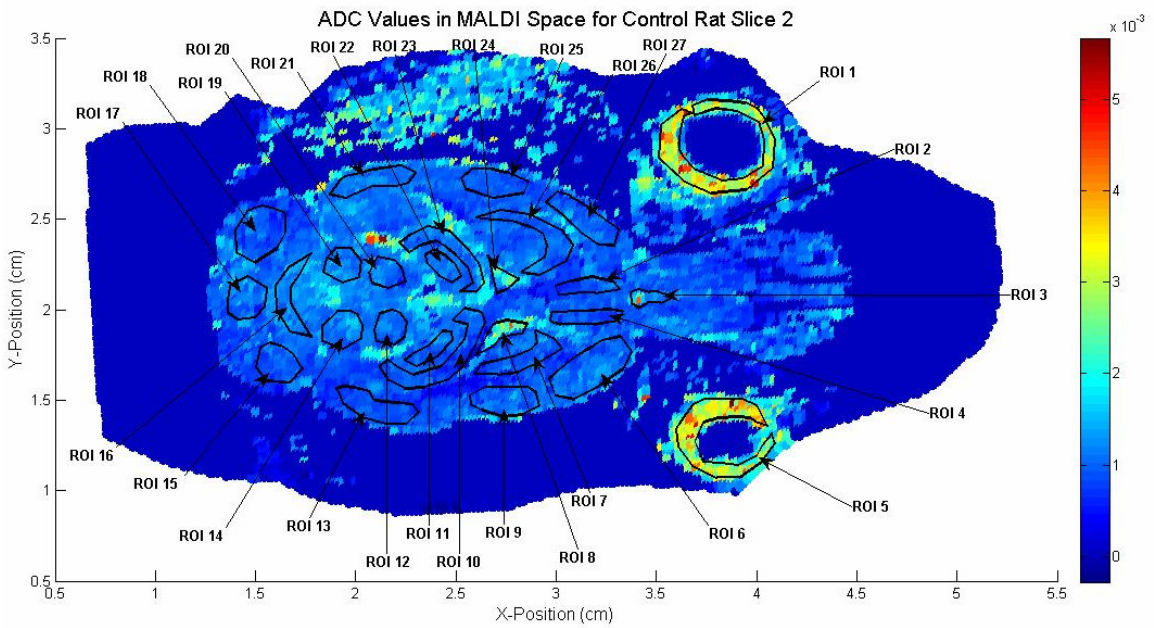

Figure 17: ROIs in ADC data translated into MALDI space for control rat slice two. The ROIs are numbered such that anatomical structures across slices are identified by identical ROI numbers.

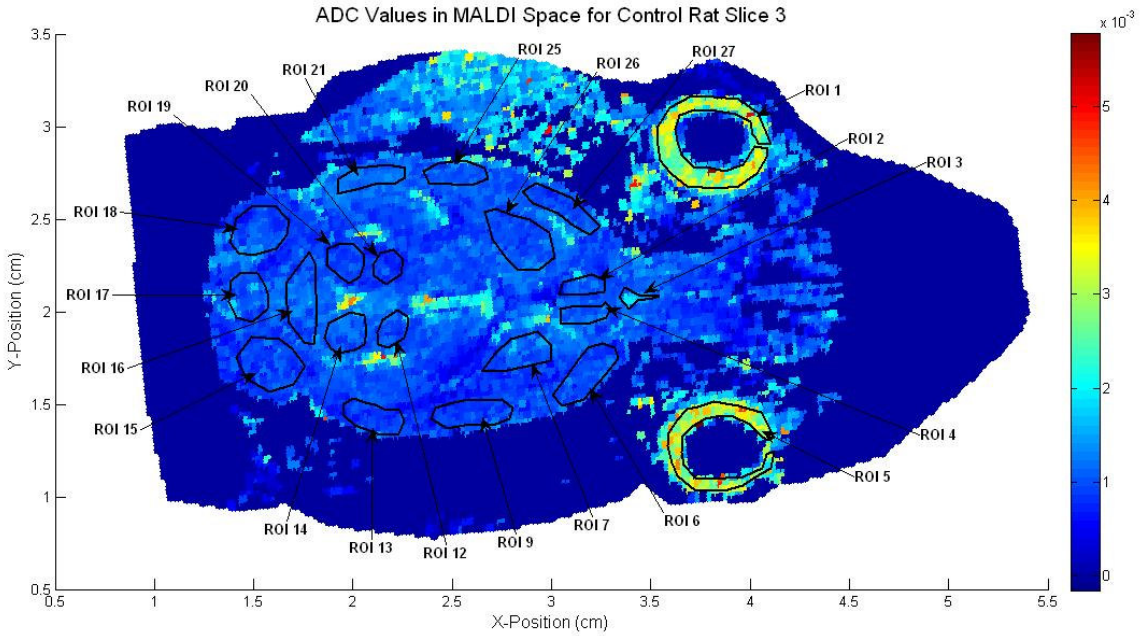

Figure 18: ROIs in ADC data translated into MALDI space for control rat slice three. The ROIs are numbered such that anatomical structures across slices are identified by identical ROI numbers. The absence of ROIs 8, 10, 11, and 22-24 in this data slice are due maintenance of a numbering scheme which identifies similar structures across slices by identical numbers. The omitted ROI numbers correspond to absence of structures at the depth of the third slice which were present in the first two slices.

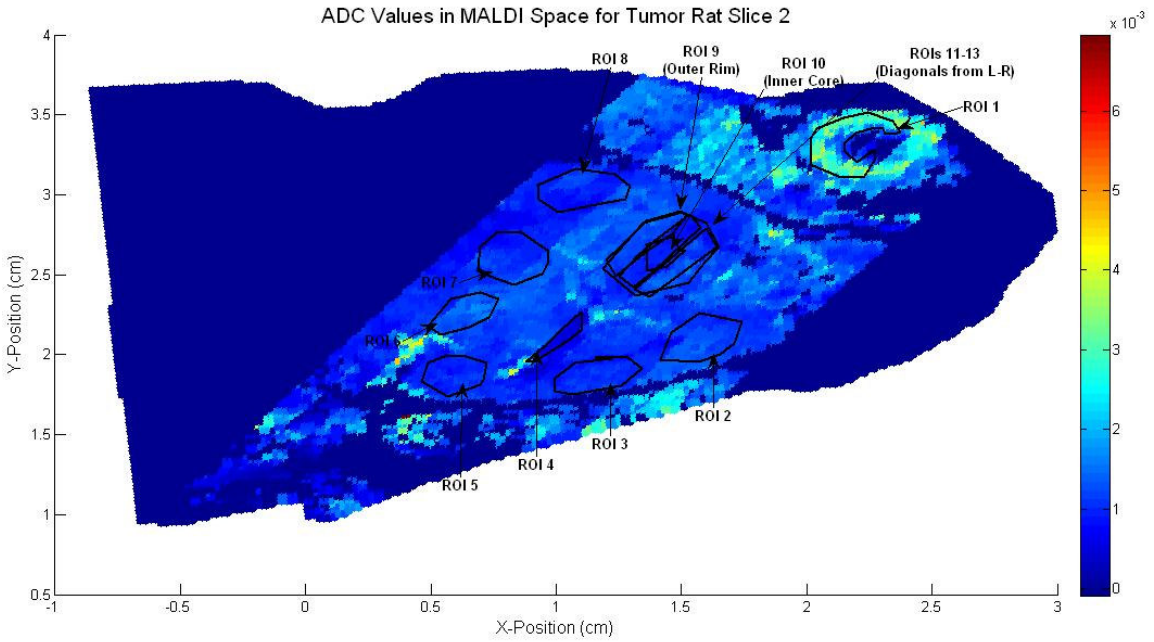

Figure 19: ROIs in ADC data translated into MALDI space for tumor rat slice two. Data quality reflects misalignment of the rat head during the two different data acquisition processes and heterogeneous MR data distributed across the resolution of the MR scanner. The diffusion rates in the ROIs of this slice were not statistically equivalent to those in the ROIs of slices one and three, necessitating the omission of this data slice from inter-slice spectral analysis.

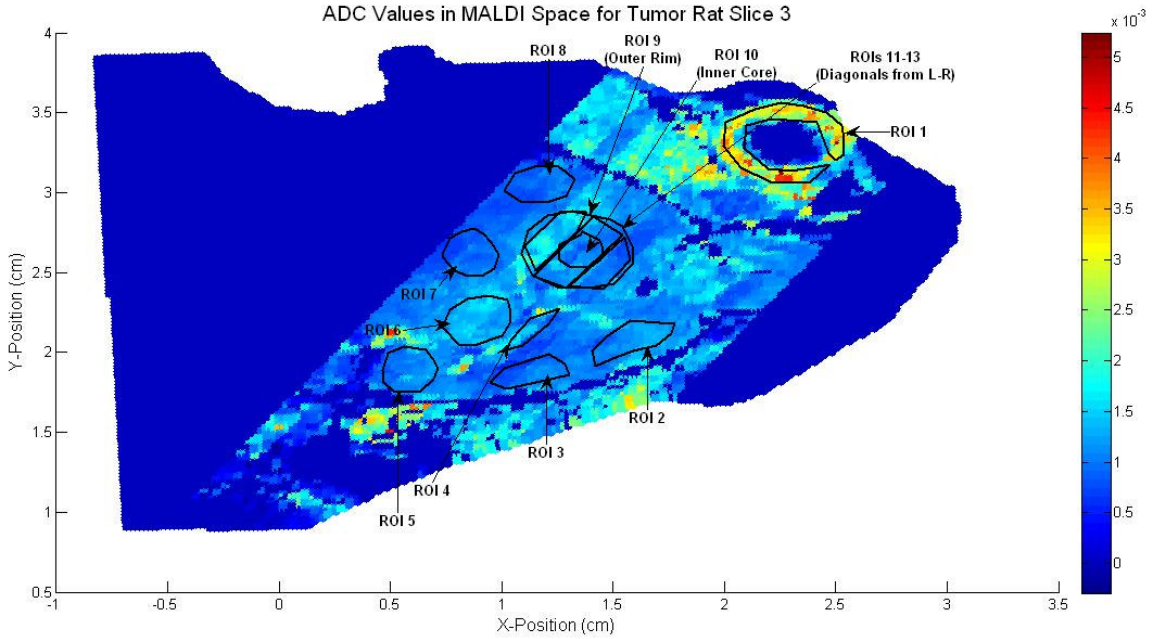

Figure 20: ROIs in ADC data translated into MALDI space for tumor slice three. Data quality reflects misalignment of the rat head during the two different data acquisition processes and heterogeneous MR data distributed across the resolution of the MR scanner.

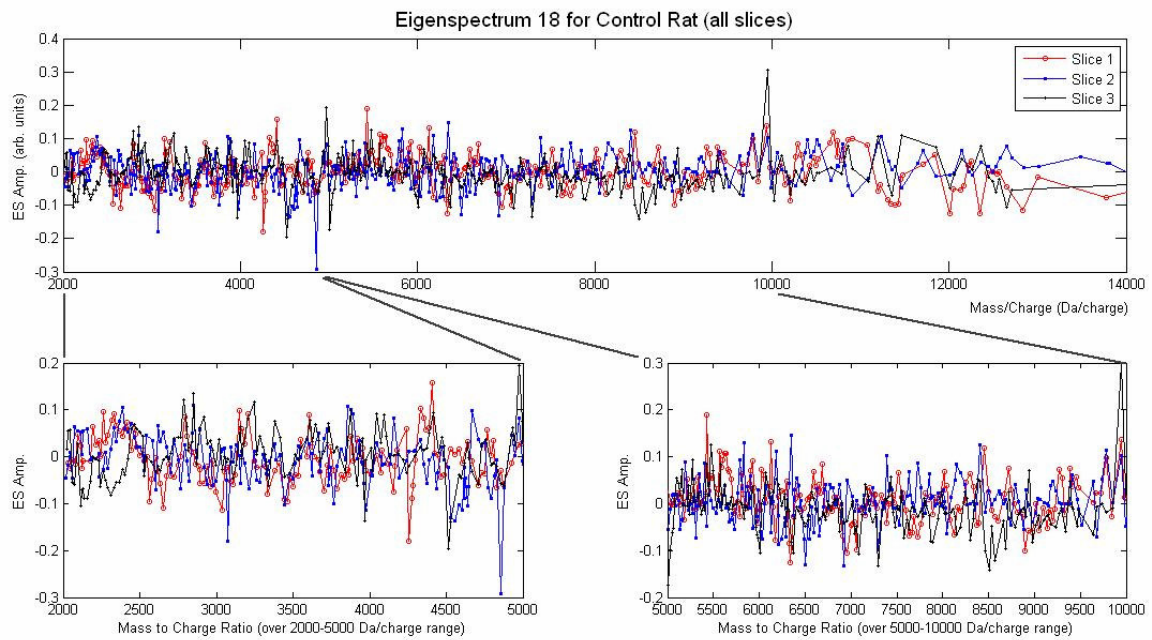

Figure 21: Control rat eigenspectrum 18 for all three slices. The corresponding eigenimage correlated with the right superior colliculus in all three slices of the control rat data (Table 3). Many peaks in this eigenspectrum share similar amplitudes, locations along the mass to charge ratio axis, or both. This suggests the presence of multiple proteins which are similar across two or more slices. However, the peaks are not as well-aligned as those in eigenspectrum 4, which correlated with the rhinal incisura, indicating a lower degree of inter-slice protein signature similarity in right superior colliculus relative to the rhinal incisura. Sensitivity falls off sharply beyond 14 kDa/charge.

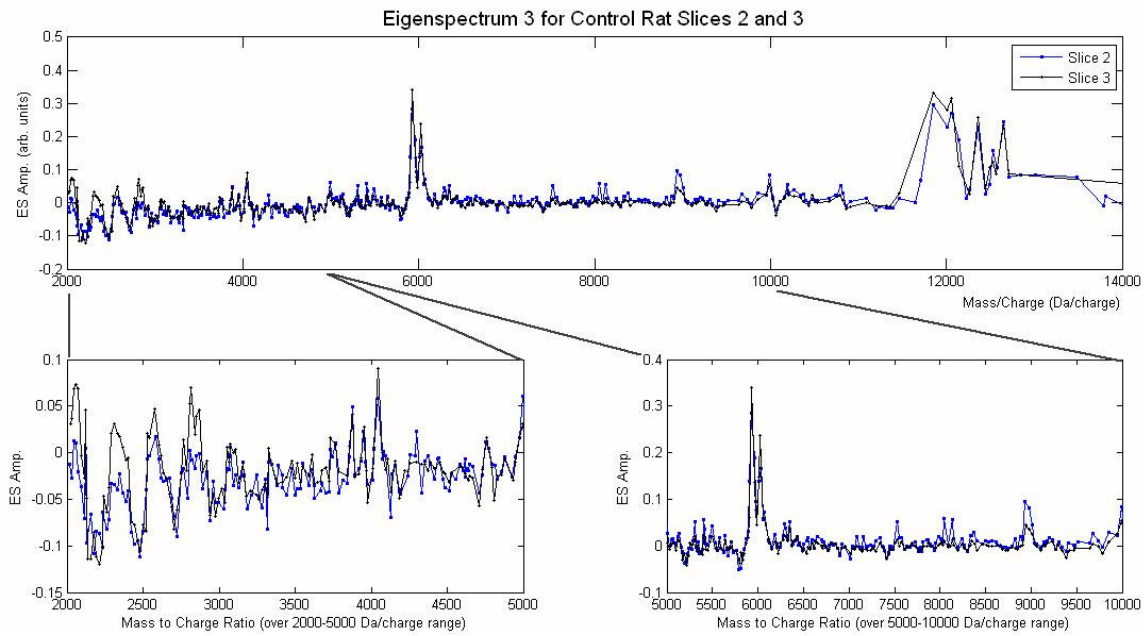

Figure 22: Control rat eigenspectrum 3 for slices 2 and 3. Eigenimage 3 correlated well with the right lateral cerebellum in the second and third slice of the control rat data (Table 3). Relative to the eigenspectra for ROIs in the rhinal incisura and right superior colliculus of the control rat, the peaks in this eigenspectrum are moderately similar in amplitude, location along the mass to charge ratio axis, or both. This suggests the presence and concentration of multiple proteins which are similar across two or more slices in cerebellum. The degree of inter-slice protein signature similarity in the cerebellum appears greater than that of the right superior colliculus , yet less than that of the rhinal incisura. Sensitivity falls off sharply beyond 14 kDa/charge.

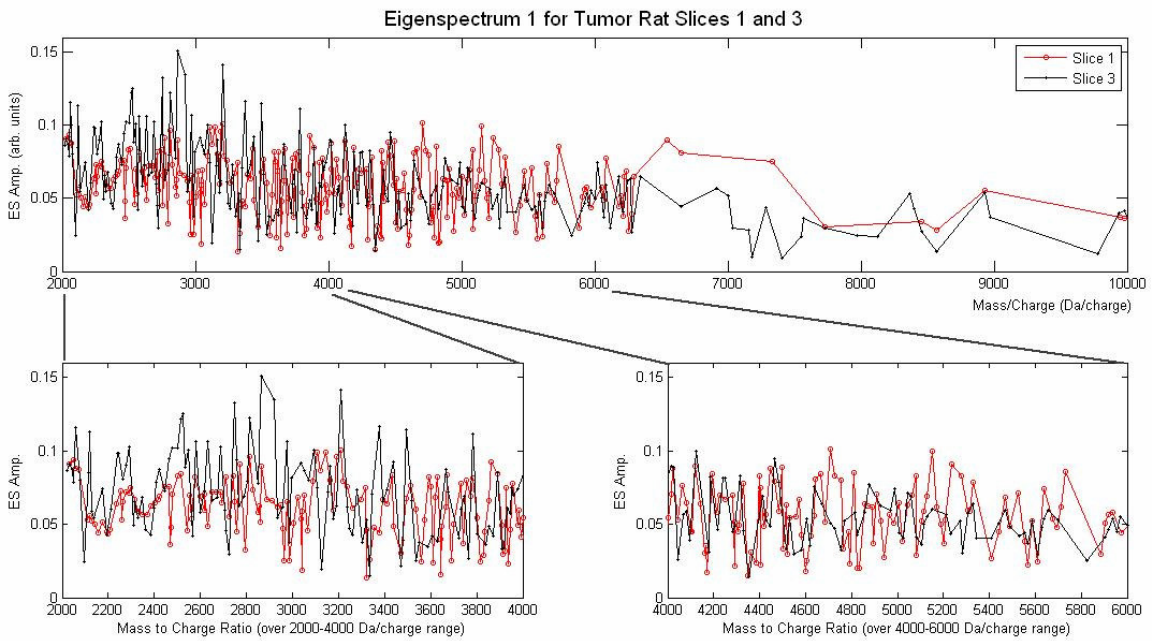

Figure 23: Tumor rat eigenspectrum 1 for slices one and three. The corresponding eigenimage correlated significantly with the right hippocampus in the tumor rat data. Throughout the range of mass to charge ratios, the peaks in each slice's eigenspectrum frequently appear with qualitatively dissimilar amplitudes. However, many points on the plots of both spectra appear at similar mass to charge ratios, suggesting that, while multiple proteins of similar mass are present in both slices of the tumor data, their concentrations in the right hippocampus of the tumor rat vary according to slice position. Sensitivity of the tumor rat MALDI data falls off sharply beyond 11 kDa/charge.

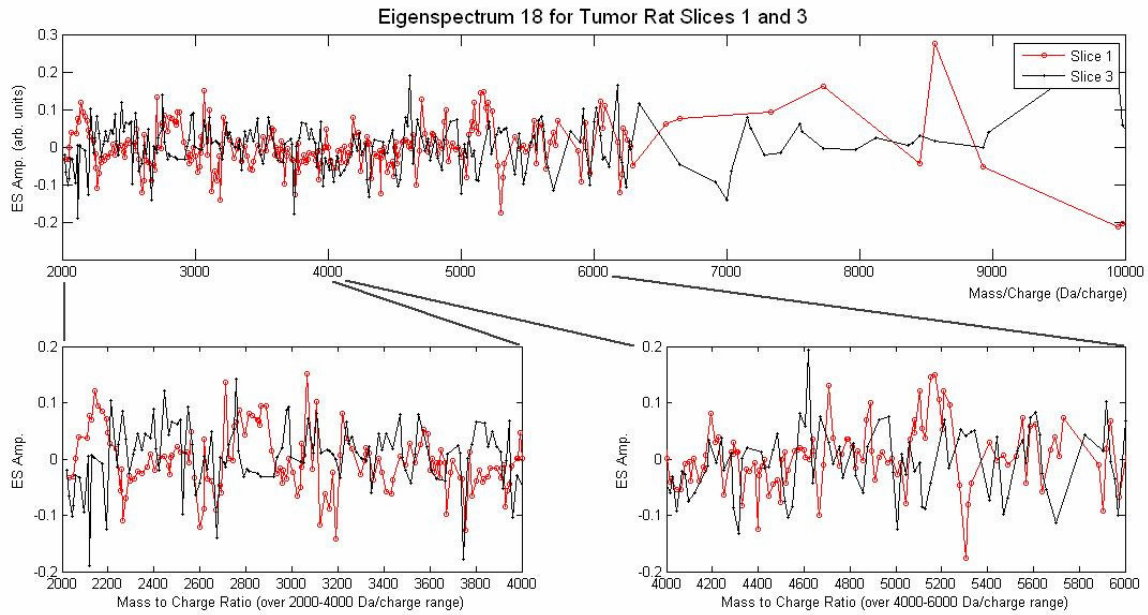

Figure 24: Tumor rat eigenspectrum 18 for slices one and three. The corresponding eigenimage correlated significantly with the mediolateral cortex in the tumor rat data. Throughout the range of mass to charge ratios, the peaks in each slice's eigenspectrum frequently appear with qualitatively dissimilar amplitudes. However, many points on the plots of both spectra appear at similar mass to charge ratios, suggesting that, while multiple proteins of similar mass are present in both slices of the tumor data, their concentrations in the mediolateral cortex of the tumor rat vary according to slice position. Sensitivity of the tumor rat MALDI data falls off sharply beyond11 kDa/charge.

B. ADDITIONAL TABLES

Table 8: T-Statistics for ADC t-test in control rat ROIs

		Rhinal Incisura			Superior Colliculus			Cerebellum	
	Slice	**1**	**2**	**3**	**1**	**2**	**3**	**2**	**3**
Rhinal Incisura	**1**	0	0.69	0.42	4.2	4.92	4.76	8.18	10.71
	2	0.69	0	0.3	3.69	4.24	4.08	6.61	8.91
	3	0.42	0.3	0	6.67	7.45	6.78	11.27	12.96
Superior Colliculus	**1**	4.2	3.69	6.67	0	1.22	1.72	-7.07	7.61
	2	4.92	4.24	7.45	1.22	0	0.72	5.87	6.49
	3	4.76	4.08	6.78	1.72	0.72	0	4.23	4.85
Cerebellum	**2**	8.18	6.61	11.27	7.07	5.87	4.23	0	0.13
	3	10.71	8.91	12.96	7.61	6.49	4.85	0.13	0

Table 9: P-Values for ADC t-test in control rat ROIs

		Rhinal Incisura			Superior Colliculus			Cerebellum	
	Slice	**1**	**2**	**3**	**1**	**2**	**3**	**2**	**3**
Rhinal Incisura	**1**	1	0.494	0.676	0.000	0.000	0.000	0.000	0.000
	2	0.494	1	0.764	0.000	0.000	0.000	0.000	0.000
	3	0.676	0.764	1	0.000	0.000	0.000	0.000	0.000
Superior Colliculus	**1**	0.000	0.000	0.000	1	0.224	0.088	0.000	0.000
	2	0.000	0.000	0.000	0.224	1	0.471	0.000	0.000
	3	0.000	0.000	0.000	0.088	0.471	1	0.000	0.000
Cerebellum	**2**	0.000	0.000	0.000	0.000	0.000	0.000	1	0.897
	3	0.000	0.000	0.000	0.000	0.000	0.000	0.897	1

Table 10: T-Statistics for ADC t-test in tumor rat ROIs

		Cortex		Hippocampus		Tumor Core	
	Slice	**1**	**3**	**1**	**3**	**1**	**3**
Cortex	**1**	0	0.45	19.31	22	3.39	5.53
	3	0.45	0	19.77	22.5	3.66	5.94
Hippocampus	**1**	19.31	19.77	0	1.37	9.16	12.4
	3	22	22.5	1.37	0	9.36	14.38
Tumor Core	**1**	3.39	3.66	9.16	9.36	0	0.05
	3	5.53	5.94	12.4	14.38	0.05	0

Table 11: P-Values for ADC t-test in tumor rat ROIs

		Cortex		Hippocampus		Tumor Core	
	Slice	**1**	**3**	**1**	**3**	**1**	**3**
Cortex	**1**	1	0.652	0.000	0.000	0.001	0.000
	3	0.652	1	0.000	0.000	0.000	0.000
Hippocampus	**1**	0.000	0.000	1	0.172	0.000	0.000
	3	0.000	0.000	0.172	1	0.000	0.000
Tumor Core	**1**	0.001	0.000	0.000	0.000	1	0.964
	3	0.000	0.000	0.000	0.000	0.964	1

REFERENCES

1. Tsai P, Shiah S, Lin M, Wu C., Kuo M. Up-regulation of Vascular Endothelial Growth Factor C in Breast Cancer Cells by Heregulin-β1. *J. Biol. Chem.* 2003; 278 (8): 5750 – 59.

2. Schwarz S, Weil R, Thompson R, Shyr Y, Moore J, Toms S, Johnson M, Caprioli R. Proteomic-Based Prognosis of Brain Tumor Patients Using Direct-Tissue Matrix-Assisted Laser Desorption Ionization Mass Spectrometry. *Cancer Res.* 2005; 65(17): 7674 – 81.

3. Floyd E, Mcshane T. Development and Use of Biomarkers in Oncology Drug Development. *Toxicol. Pathol.* 2004; 32: 106 – 15.

4. Begent, RH. Interpretation of Treatment Results with Biological Agents: Is There a Need for a New Methodology? *J. of B.U.ON.* 2007; 12(1): 53 – 58.

5. Sinha T, Khatib-Shahidi S, Yankeelov T, Mapara K, Ehtesham M, Cornett D, Dawant B, Caprioli R, Gore J. Integrating Spatially Resolved Three Dimensional MALDI IMS with *in vivo* Magnetic Resonance Imaging. *Nature Methods*, 2008; 5(1): 57 – 59.

6. American Cancer Society. *Cancer Facts & Figures 2008*. Atlanta: American Cancer Society; 2008.

7. American Cancer Society. *Cancer Facts & Figures 2007.* Atlanta: American Cancer Society; 2007.

8. Grobben B, De Deyn P, Slegers H. Rat C6 Glioma as Experimental Model System for the Study of Glioblastoma Growth and Invasion. *Cell Tissue Res.* 2002; 310: 257 – 70.

9. Pestalozzi BC, Peterson HF, Gelber RD, Goldhirsch A, Gusterson BA, Trihia H, Lindtner J, Cortes-Funes H, Simmoncini E, Byrne MJ, Golouh R, Rudenstam CM, Castiglione-Gertsch M, Allegra CJ, Johnston PG. Prognostic Importance of Thymidylate Synthase Expression in Early Breast Cancer. *J. Clin. Onc.* 1997; 15(5): 1923 – 31.

10. Glunde K, Jacobs M, Bhujwalla Z. Choline Metabolism in Cancer: Implications for Diagnosis and Therapy. *Expert Rev. Mol. Diagn* 2006; 6(6):821 – 29.

11. Glunde K, Serkova J. Therapeutic Targets and Biomarkers Identified in Cancer Choline Phospholipid Metabolism. *Pharmacogenomics*. 2006; 7(7):1109 – 23.

12. Bartella L, Huang W. Proton (^{1}H) MR Spectroscopy of the Breast. *RadioGraphics* 2007; 27: S241 – 52.

13. Lin E, Li J, Gnatovskiy L, Deng Y, Zhu L, Grzesik D, Qian H, Xue X, Pollard J. Macrophages Regulate the Angiogenic Switch in a Mouse Model of Breast Cancer. *Cancer Res.* 2006; 66 (23):11238 – 46.

14. Gupta M, Qin R. Mechanism and Its Regulation of Tumor-Induced Angiogenesis. *World J. Gastroenterol.* 2003; 9(6):1144 – 55.

15. Valable S, Lemasson B, Farion R, Beaumont M, Segebarth C, Remy C, Barbier E. Assessment of Blood Volume, Vessel Size, and the Expression of Angiogenic Factors in Two Rat Glioma Models: A Longitudinal *in vivo* and *ex vivo* Study. *NMR Biomed*. 2008; 21(10):1043 – 56.

16. Oh J, Henry R, Pirzkall A, Lu Y, Li X, Catalaa I, Chang S, Dillon W, Nelson S. Survival Analysis in Patients with Glioblastoma Multiforme: Predictive Value of Choline-to-NAcetylaspartate Index, Apparent Diffusion Coefficient, and Relative Cerebral Blood Volume. *J. Magn. Reson. Imag.* 2004; 19: 546 – 54.

17. Chenevert T, Sundgren P, Ross B. Diffusion Imaging: Insight to Cell Status and Cytoarchitecture. *Nueroimag. Clin. N. Am.* 2006; 16: 619 – 32.

18. Barboriak D. Imaging of brain tumors with diffusion-weighted and diffusion tensor MR imaging. *Magn. Reson. Imag. Clin. N. Am.* 2003; 11(3): 379 – 401.

19. Maier S, Bogner P, Bajzik G, Mamata H, Mamata Y, Repa I, Jolesz F, Mulkern R. Normal Brain and Brain Tumor: Multicomponent Apparent Diffusion Coefficient Line Scan Imaging. *Radiology* 2001**;** 219: 842 – 849.

20. Guo Y, Cai Y, Cai Z, Gao Y, An N, Ma L, Mahankali S, Gao J. Differentiation of clinically benign and malignant breast lesions using diffusion-weighted imaging. *J. Magn. Reson. Imag.* 2002; 16(2): 172 – 78.

21. Hayashida Y, Hirai T, Morishita S, Kitajima M, Murakami R, Korogi Y, Makino K, Nakamura H, Ikushima I, Yamura M, Kochi M, Kuratsu J, Yamashita Y. Diffusion-weighted imaging of metastatic brain tumors: comparison with histologic type and tumor cellularity. *Am. J. Neuroradiol.* 2006; 27(7):1419 – 25.

22. Manenti G, Roma M, Mancino S, Bartolucci D, Palmieri G, Mastrangeli R, Miano R, Squillaci E, Simonetti G. Malignant renal neoplasms: correlation between ADC values and cellularity in diffusion weighted magnetic resonance imaging at 3 T. *Radiol. Med.* 2008; 113(2):199 – 213.

23. Anderson A, Xiea J, Pizzonia J, Bronen R, Spencer D, Gore J. Effects of Cell Volume Fraction Changes on Apparent Diffusion in Human Cells. *Magn. Reson. Imaging*. 2000; 18(6): 689–95.

24. Sugahara T, Korogi Y, Kochi M, Ikushima I, Shigematu Y, Hirai T, Okuda T, Liang L, Ge Y, Komohara Y, Ushio Y, Takahashi M. Usefulness of diffusion-weighted MRI with echo-planar technique in the evaluation of cellularity in gliomas. *J. Magn. Reson. Imag.* 1999; 9(1): 53 – 60.

25. Luypaert R, Boujraf S, Sourbron S, Osteaux M. Diffusion and Perfusion MRI: Basic Physics. *Eur. J. Rad.* 2001; 38: 19 – 27.

26. Le Bihan D, Breton E, Lallemand D, Grenier P, Cabanis E, Laval-Jeantat M. MR Imaging of Intravoxel Incoherent Motions: Application to Diffusion and Perfusion in Neurologic Disorders. *Radiology* 1986; 161:401-407.

27. Hendee W, Ritenour E. *Medical Imaging Physics*. 4th ed. New York: Wiley-Liss, 2002.

28. Chenevert T, Stegman L, Taylor J, Robertson P, Greenberg H, Rehemtulla A, Ross B. Diffusion Magnetic Resonance Imaging: an Early Surrogate Marker of Therapeutic Efficacy in Brain Tumors. *J. Nat. Cancer Inst*. 2000; 92(4): 2030 – 36.

29. Le Bihan D. Molecular Diffusion, Tissue Microdynamics and Microstructure. *NMR in Biomed*. 1995; 8: 375 – 86.

30. Charles-Edwards E, deSouza N. Diffusion-Weighted Magnetic Resonance Imaging and Its Application to Cancer. *Cancer Imaging* 2006; 6: 135 – 43.

31. Chen F, De Keyzer F, Wang H, Vandecaveye V, Landuyt W, Bosmans H, Hermans R, Marchal G, Yicheng N. Diffusion Weighted Imaging in Small Rodents Using Clinical MRI Scanners. *Methods* 2007; 43: 12 – 20.

32. Fan G, Zang P, Jing F, Wu Z, Guo Q. Usefulness of Diffusion/Perfusion-weighted MRI in Rat Gliomas: Correlation with Histopathology. *Acad Radiol* 2005**;** 12: 640 – 51.

33. Zhang J, van Zijl P, Laterra J, Salhotra A, Lal B, Mori S, Zhou J. Unique Patterns of Diffusion Directionality in Rat Brain Tumors Revealed by High-Resolution Diffusion Tensor MRI. *Mag. Res. in Med.* 2007; 58: 454 – 62.

34. Kim S, Pickup S, Hsu O, Poptani H. Diffusion Tensor MRI in Rat Models of Invasive and Well-Demarcated Brain Tumors. *NMR Biomed*. 2008; 21: 208 – 16.

35. Lope-Piedrafita S, Garcia-Martin M, Galons J, Gillies R, Trouard T. Longitudinal Diffusion Tensor Imaging in a Rat Brain Glioma Model. *NMR Biomed.* 2008; 21(8):799 – 808.

36. Bennett K, Hyde J, Rand S, Bennett R, Krouwer H, Rebro K, Schmainda K. Intravoxel Distribution of DWI Decay Rates Reveals C6 Glioma Invasion in Rat Brain. *Magn. Reson. Med.* 2004; 52(5): 994 – 1004.

37. Provenzale J, Mukundan S, Barboriak D. Diffusion-weighted and Perfusion MR Imaging for Brain Tumor Characterization and Assessment of Treatment Response. *Radiology* 2006; 239(3): 632 – 49.

38. Firat A, Karakas H, Erdem G, Yakinci C, Bicak U. Diffusion Weighted MR Findings of Brain Involvement in Tuberous Sclerosis. *Diagn. Interv. Radiol.* 2006; 12: 57 – 60.

39. Burdette J, Durden D, Elster D, Yen Y. High *b*-Value Diffusion-Weighted MRI of Normal Brain. *J. Comput. Assist. Tomogr.* 2001; 25(4): 515 – 19.

40. Pradeep C, Sunila E, Kuttan G. Expression of Vascular Endothelial Growth Factor (VEGF) and VEGF Receptros in Tumor Angiogenesis and Malignancies. *Integrative Cancer Therapies*. 2005; 4(4): 315 – 21.

41. Stuart-Harris R, Caldas C, Pinder S, Pharoah P. Proliferation Markers and Survival in Early Breast Cancer: A Systematic Review and Meta-analysis of 85 Studies in 32,825 Patients. *The Breast*. 2008; 17: 323 – 34.

42. Fidler I. Critical Determinants of Metastasis. *Sem. Cancer Bio*. 2002; 12: 89 – 96.

43. Urruticoechea A, Smith I, Dowsett M. Proliferation Marker Ki-67 in Early Breast Cancer. *J. Clin. Onc.* 2005; 23(28): 7212 – 20.

44. Caldwell R, Caprioli R. Tissue Profiling by Mass Spectrometry: A Review of Methodology and Applications. *Mol. Cell Proteomics* 2005; 4: 394 – 401.

45. Reyzer M, Caprioli R. MALDI Mass Spectrometry for Direct Tissue Analysis: A New Tool for Biomarker Discovery. *J. Proteome Res*. 2005; 4:1138 – 1142.

46. Fitzgerald M, Smith L. Mass Spectrometry of Nucleic Acids: The Promise of Matrix-Assisted Laser Desorption-Ionization (MALDI) Mass Spectrometry. *Annu. Rev. Biophys. Biomol. Struct.* 1995; 24: 117 – 40.

47. Baldwin M. Mass Spectrometers for the Analysis of Biomolecules. *Meth. Enzym*. 2005; 402: 3 – 48.

48. Coombes K, Koomen J, Baggerly K, Morris J, Kobayashi R. Understanding the Characteristics of Mass Spectrometry Data through the Use of Simulation. *Cancer Informatics* 2005; 1: 41 – 52.

49. Serway R, Beichner R, Jewett, J. *Physics for Scientists and Engineers.* 5th ed. Thomson Learning, 2000.

50. Linke T, Doraiswamya S, Harrison E. Rat plasma proteomics: Effects of Abundant Protein Depletion on Proteomic Analysis. *J. Chromatography* 2007; 849: 273 – 81.

51. Ross M, Filipovska A, Smith R, Gait M, Murphy M. Cell-Penetrating Peptides Do Not Cross Mitochondrial Membranes Even When Conjugated to a Lipophilic Cation: Evidence Against Direct Passage through Phospholipid Bilayers. *Biochem. J*. 2004; 383: 457 – 68.

52. Caprioli R, Farmer T, Gile J. Molecular Imaging of Biological Samples: Localization of Peptides and Proteins Using MALDI-TOF MS. *Anal. Chem.* 1997; 69: 4751 – 60.

53. Van de Plas R, Ojeda F, Dewil M, Van Den Bosch L, De Moor B, Waelkens E. Prospective Exploration of Biochemical Tissue Composition *via* Imaging Mass Spectrometry Guided By Principal Component Analysis. *Pac. Symp. Biocomp*. 2007; 12: 458 – 69.

54. Berrar D, Dubitzky W, Granzow M (Eds). *A Practical Approach to Microarray Data Analysis*. Norwell, MA: Kluwer, 2003.

55. Zou K, Tuncali K, Silverman S. Correlation and Simple Linear Regression. *Radiology* 2003; 227:617 – 628.

56. Lohninger H. Teach/Me Data Analysis, Springer-Verlag, Berlin-New York-Tokyo, 1999.

57. Hajnal J, Hill D, Hawkes D (Eds). *Medical Image Registration.* New York: CRC, 2001.

58. Paxinos G, Watson, C. *The Rat Brain in Stereotaxic Coordinates.* 4th ed. San Diego: Academic Press, 1998.

59. Knochenmuss R. Ion Formation Mechanisms in UV-MALDI. *Analyst* 2006; 131: 966–86.

60. Zhuang H, Wuarin L, Fei Z, Ishii D. Insulin-Like Growth Factor (IGF) Gene Expression Is Reduced in Neural Tissues and Liver from Rats with Non-Insulin-

Dependent Diabetes Mellitus, and IGF Treatment Ameliorates Diabetic Neuropathy. *J. Pharm. and Exp. Therapeutics* 1997; 238 (1): 366 – 74.

61. Haselbacher G, Schwab M, Pasi A, Humbel R. Insulin-Like Growth Factor II (IGF II) in Human Brain: Regional Distribution of IGF II and of Higher Molecular Mass Forms. *Proc. Nati. Acad. Sci.* 1985; 82: 2153 – 57.

62. Ostenson C, Ahrén B, Karlsson S, Knudsen J, Efendic S. Inhibition by Rat Diazepam-Binding Inhibitor/Acyl-Coa-Binding Protein of Glucose-Induced Insulin Secretion in the Rat. *Eur. J. of Endocrinology* 1994; 131 (2): 201 – 204.

63. Dasu M, Herndon D, Spies M, Perez-Polo J. Genomic Analysis of Insulin-Like Growth Factor-I Gene Transfer in Thermally Injured Rats. *Wound Rep. Reg.* 2004; 12: 217 – 224.

64. Bohrer B, Merenbloom S, Koeniger S, Hilderbrand A, Clemmer D. Biomolecule Analysis by Ion Mobility Spectrometry. *Annu. Rev. Anal. Chem*. 2008; 1:10 – 35.

65. Vannucci S, Mummery R, Hawkes R, Rider C, Beesley P. Hypoxia-Ischemia Induces a Rapid Elevation of Ubiquitin Conjugate Levels and Ubiquitin Immunoreactivity in the Immature Rat Brain. *J. of Cerebral Blood Flow & Metabolism* 1998; 18: 376–385.

66. Glatz J, van der Vusse G. Cellular Fatty Acid-Binding Proteins: Current Concepts and Future Directions. *Mol. and Cell. Biochem.* 1990; 98: 237 – 51.

67. Schaub M, Heizmann C. Calcium, Troponin, Calmodulin, S100 Proteins: From Myocardial Basics to New Therapeutic Strategies. *Biochem. and Biophys. Res. Comm*. 2008; 369: 247 – 264.

68. Liu X, Kim CN, Yang J, Jemmerson R, Wang X. Induction of Apoptotic Program in Cell-Free Extracts: Requirement for Datp and Cytochrome C. *Cell* 1996; 86(1):147 – 57.

69. Nakajo S, Omata K, Aiuchi T, Shibayama T, Okahashi I, Ochiai H, Nakai Y, Nakaya K, Nakamura Y. Purification and Characterization of a Novel Brain-Specific 14-kDa Protein. *J. of Neurochemistry* 1990; 55 (6): 2031 – 38.

70. Kaur P, Raheja G, Singh S, Gill K. Purification and Characterization of Neuropathy Target Esterase (NTE) from Rat Brain. *Life Sciences* 2006; 78: 2967 – 73.

71. Kodera T, Nakagawa T, Kubota T, Kabuto M, Sato K, Kobayashi H. The Expression and Activation of Matrix Metalloproteinase-2 in Rat Brain after Implantation of C6 Rat Glioma Cells. *J. of Neurooncol.* 2000; 46 (2): 105 – 14.

72. Sevigny M, Silva J, Lan W, Alano C, Swanson R. Expression and Activity of Poly(ADP-ribose) Glycohydrolase in Cultured Astrocytes, Neurons, and C6 Glioma Cells. *Mol. Brain Res.* 2003; 117: 213 – 220.

73. Carmeliet, P. VEGF as a Key Mediator of Angiogenesis in Cancer. *Oncology* 2005; 69 (suppl 3): 4–10.

74. Morrone F, Oliveira D, Gamermann P, Stella J, Wofchuk S, Wink M, Meurer L, Isabel M, Edelweiss A, Lenz G, O Battastini A. *In Vivo* Glioblastoma Growth Is Reduced by Apyrase Activity in a Rat Glioma Model. *BMC Cancer* 2006; 6: 226 – 36.